Synaptotagmin 7 transiently docks synaptic vesicles to support facilitation and Doc2α-triggered asynchronous release

Zhenyong Wu[1,2†#], Grant F. Kusick[3,4†], Manon M. M. Berns[5], Sumana Raychaudhuri[3], Kie Itoh[3], Alexander M. Walter[5,6], Edwin R. Chapman[1,2*] & Shigeki Watanabe[3,7*]

[1]Department of Neuroscience, University of Wisconsin-Madison, Madison, USA
[2]Howard Hughes Medical Institute, Madison, USA
[3]Department of Cell Biology, Johns Hopkins University, School of Medicine, Baltimore, MD, USA.
[4]Biochemistry, Cellular and Molecular Biology Graduate Program, Johns Hopkins University, School of Medicine, Baltimore, MD, USA.
[5]Department of Neuroscience, University of Copenhagen, Copenhagen, Denmark
[6]Molecular and Theoretical Neuroscience, Leibniz-Institut für Molekulare Pharmakologie, FMP im CharitéCrossOver, Berlin, Germany
[7]Solomon H. Snyder Department of Neuroscience, Johns Hopkins University, School of Medicine, Baltimore, MD, USA

[*]Corresponding author. Email: shigeki.watanabe@jhmi.edu, chapman@wisc.edu

[†]These authors contributed equally to the manuscript

#Current institution: Shanghai Institute of Materia Medica, Chinese Academy of Sciences, Shanghai, China

Abstract: The molecular basis of asynchronous neurotransmitter release remains enigmatic despite decades of intense study. Synaptotagmin (syt) 7 and Doc2 have both been proposed as Ca^{2+} sensors that trigger this mode of exocytosis, but conflicting findings have led to controversy. Here, we demonstrate that at excitatory mouse hippocampal synapses, Doc2α is the major Ca^{2+} sensor for asynchronous release, while syt7 supports this process through activity-dependent docking of synaptic vesicles. In synapses lacking Doc2α, asynchronous release after single action potentials is strongly reduced, while deleting syt7 has no effect. However, in the absence of syt7, docked vesicles cannot recover on millisecond timescales. Consequently, both synchronous and asynchronous release depress from the second pulse on during repetitive activity. By contrast, synapses lacking Doc2α have normal activity-dependent docking, but continue to exhibit decreased asynchronous release after multiple stimuli. Moreover, disruption of both Ca^{2+} sensors is non-additive. These findings result in a new model whereby syt7 drives activity-dependent docking, thus 'feeding' synaptic vesicles to Doc2 for asynchronous release during ongoing transmission.

Main Text:

Ca^{2+}-triggered neurotransmitter release involves at least two kinetically distinct components: one synchronous, which sets in after tens of microseconds (1) of a stimulus and completes within several milliseconds, and another asynchronous, which sets in more slowly and can persist for tens or hundreds of milliseconds (2, 3). The molecular basis of synchronous release has been characterized in depth, and there is broad agreement that the underlying Ca^{2+} sensors are two members of the synaptotagmin (syt) family of proteins, isoforms 1 and 2 (4). The Ca^{2+} sensors that regulate asynchronous release (AR), however, remain a subject of controversy.

AR is thought to play a critical role in information processing and circuit function (2, 5, 6) and has been implicated in epileptiform activity in rats and humans (7). However, it is impossible to directly test how slow transmission impacts neural networks without knowing what proteins are specifically required for AR.

Two classes of proteins have been proposed as Ca^{2+} sensors for AR in vertebrates: Doc2 and syt7. Two isoforms of Doc2, α and β function as Ca^{2+} sensors; α mediates AR in hippocampal neurons, and loss of AR in α knockout (KO) neurons can be rescued by β (8). Both Doc2 and syt7 exhibit the slow Ca^{2+}-regulated membrane-binding kinetics and high affinity required for AR (8–10). In cultured hippocampal neurons, we previously found that Doc2α drives significant levels of AR both after single action potentials and during trains (8, 9, 11, 12). This activity depends on calcium binding (9, 12). However, no significant changes in AR were observed in Purkinje cell to deep cerebellar nuclei synapses (13) and in autaptic cultured hippocampal neurons lacking Doc2 (14). These varying results have left the importance of Doc2 for AR in doubt.

Syt7 has received more attention (15), but its exact role in AR is still uncertain. Syt7 is important for AR at the zebrafish neuromuscular junction (16). However, conflicting evidence has accumulated for mammalian central synapses. In syt7 KO mouse cortical neurons, no synaptic phenotypes were initially observed (17). Later studies found defects in AR when deleting syt7 or preventing it from binding Ca^{2+}– in cultured hippocampal neurons (18), inhibitory synapses formed between basket cells and Purkinje neurons as well as granule cell synapses in the cerebellum (19, 20), and in excitatory synapses between pyramidal cells and Martinotti neurons in the neocortex (21). However, unlike Doc2α, the role of syt7 in AR is usually only apparent when more than one stimulus is applied. Among these studies, deleting syt7 decreased AR—after a single action potential—only in granule cell synapses (20) and in syt1 KO cultured hippocampal neurons (18). In inhibitory synapses of the inferior olive, where release after single action potentials is often highly asynchronous, deleting syt7 actually makes release even slower (22). Thus, the importance of syt7 and Doc2α in AR may depend, at least in part, on the frequency of stimulation, the number of stimuli applied, and the synapse under study. The reason for these differences is unknown, reflecting a lack of mechanistic insight into how these proteins support AR.

To test how Doc2α and syt7 mediate AR, we performed glutamate sensor imaging and electrophysiology experiments in single and double knockout mouse hippocampal neurons. We

then explored how these sensors act on synaptic vesicles using zap-and-freeze electron microscopy and mathematical modeling. In both cultured neurons and acute slices, AR after single action potentials was strongly reduced in Doc2α KOs, but not in syt7 KOs, suggesting that Doc2α more directly mediates AR. In contrast, AR during train stimulation was reduced to a similar extent in both syt7 and Doc2α KO neurons. Ultrastructural analysis revealed that, in syt7 KO neurons, docked synaptic vesicles fail to recover on millisecond timescales (23). Consequently, both synchronous and asynchronous release quickly and profoundly depress during train stimulation. By contrast, in Doc2α KO neurons this syt7-dependent ultrafast recruitment of vesicles was unaffected. Thus, with AR largely absent, more newly-recruited vesicles are available for synchronous release, leading to slower depression in Doc2α KO neurons. AR in Doc2α /syt7 DKO neurons was similar to Doc2α KO. Our findings are consistent with a sequential model wherein synaptic vesicle docking, but not fusion, is facilitated by syt7 during activity, while syt1 and Doc2α act downstream and compete with each other to trigger exocytosis. Overall, we propose that during repetitive stimulation, syt7 supplies docked vesicles for synchronous release and Doc2α-mediated AR.

Results

Doc2α, but not syt7, mediates asynchronous release in response to single action potentials

To directly monitor glutamate release, we transduced an optical glutamate reporter (iGluSnFR) into cultured mouse hippocampal neurons (*24*, *25;* Fig. 1A,B and Fig. S1). This approach bypasses postsynaptic factors that influence the time course of transmission as monitored using traditional patch-clamp recordings and allows individual AR events to be measured directly (26). We applied single stimuli and monitored the timing of glutamate release at the single-bouton level (Fig. 1C) from Doc2α knockout (KO, $Doc2\alpha^{em1Smoc/em1Smoc}$; Sakaguchi et al., 1999) and syt7 KO ($Syt7^{tm1Nan/tm1Nan}$; Chakrabarti et al., 2003) neurons and their respective wild-type littermates (WT – $Doc2\alpha^{+/+}$ or $Syt7^{+/+}$). We used a medium affinity iGluSnFR (A184V; K_D = 40 μM) for these single-stimulus experiments (25). Due to the fast activation kinetics of this sensor, compared to its relatively slow relaxation rate (25, 29; Fig. S1B), the timing of each release event was quantified by measuring the time-to-peak of each response. These data were plotted as histograms using 10 ms bins (Fig. 1A,B and Fig. S1 A). Peaks detected at the 10 ms time point were defined as the synchronous component of release, and all later peaks were defined as asynchronous release events (29).

In WT neurons, 64% of release events occurred at the first 10 ms time point (synchronous release: n = 1000 release events); the rest of the events (36%) were defined as asynchronous (Fig. 1C). This approach was validated by analyzing release from WT neurons treated with EGTA-AM, which reduces AR by chelating residual Ca^{2+} (30). This treatment greatly reduced AR (Fig. 1C, 88% in the first bin, 11 % in the second, and 1% in the third), consistent with previous work using this approach (29). Syt7 KO neurons had no apparent phenotype (Fig.

1C,D; 66% synchronous and 34% asynchronous, p = 0.39). The 2% reduction in AR in the KO did not reach statistical significance here, but we note that this small effect is consistent with our earlier measurements using iGluSnFR (26). By contrast, the asynchronous component was markedly reduced in Doc2α KO neurons (Fig. 1B,C; 84% synchronous and 16% asynchronous). While the amount of AR in Doc2α KO was slightly greater than in EGTA-treated WT neurons, this difference was not statistically significant (p = 0.12). The peak average fluorescence intensity in both mutants was similar to WT (Fig. S1C), demonstrating that synchronous release is not affected in these mutants (8, 26). These findings indicate that Doc2α, but not syt7, plays an important role in AR in response to a single stimulus.

We next turned to acute hippocampal slices to assay Doc2α and syt7 function in a more native circuit. We applied a single stimulus to Schaffer collaterals and measured evoked excitatory postsynaptic currents (EPSCs) from CA1 neurons by whole-cell patch clamp (Fig. 2A, and S4). As with iGluSnFR imaging in cultured neurons (Fig. 1), syt7 KOs showed no phenotype – the amplitude and kinetics of EPSCs were nearly identical to those of WT (Fig. 2B-D). By contrast, in Doc2α KO, the EPSC amplitude was unchanged, but the total charge transfer was reduced by 35% (Fig. 2B-D). Cumulative charge transfer data were fitted with double exponential functions, reflecting two kinetic components of release (Fig. 2C; (3)). The fast component, representing synchronous release, was similar across all three genotypes. However, the slow, asynchronous component was reduced by 61% in Doc2α KO neurons ($p<0.0001$); no changes in the asynchronous component were observed in syt 7 KOs (Fig. 2D). EGTA-AM treatment of WT slices reduced the slow component slightly more severely than Doc2α KO (Fig. 2B-D; p = 0.03 against Doc2α KO). Finally, the time constants for both components of evoked EPSCs were similar across all genotypes (Fig. 2D). Together, these data further indicated that AR after single action potentials is driven by Doc2α, but not syt7, in excitatory mouse hippocampal synapses.

Both Doc2α and syt7 are important for asynchronous release after repeated action potentials

We then addressed the roles of Doc2α and syt7 in AR during train stimulation. Fifty stimuli, at 10 and 20 Hz, were applied to cultured hippocampal neurons that expressed iGluSnFR responses (Fig. 3A,B). To temporally resolve the response from each pulse during the train, we used a faster, lower-affinity version of iGluSnFR (S72A; K_D = 200 μM; Marvin et al., 2018; Vevea et al., 2021). Due to its lower sensitivity, this sensor underestimates the fraction of AR as compared to the A184V used above, but its faster kinetics were essential to resolve individual peaks during train stimulation. At both 10 and 20 Hz, WT neurons exhibited slight facilitation of synchronous release (measured as the peak average fluorescence intensity) in response to the second pulse, and thereafter depressed as the train went on, eventually reaching a steady state (Fig. 3B, D, and S2A). In addition, the asynchronous fraction gradually increased during the train at both stimulation frequencies (Fig. 3C and S2B). We examined the first two responses in the train and found that paired pulse facilitation was similar between WT and Doc2α KO neurons (WT: 1.04 ±

0.06, Doc2α KO: 1.03 ± 0.04, p=0.9953, with an interstimulus interval (Δt) = 100 ms; WT: 1.31 ± 0.08, Doc2α KO: 1.28 ± 0.08, p>0.9191, Δt = 50 ms; Fig. S2B). However, in KO neurons, synaptic depression set in more slowly from the third action potential onward, eventually reaching the same steady-state depression as WT later in the train. This is consistent with the idea that the sensors for synchronous and asynchronous release compete with each other, so that reducing AR promotes sustained synchronous release (8, 31).

In contrast, syt7 KO neurons displayed paired pulse depression instead of facilitation (syt7 KO: 0.57 ± 0.03, p < 0.0001, Δt = 100 ms; syt7 KO: 0.52 ± 0.03, p < 0.0001, Δt = 50 ms; Fig. S2B), as well as faster and more severe synaptic depression as the train progressed (Fig. 3D), consistent with previous reports (19, 26, 32, 33). As in the single-stimulus measurements (Fig. 1), AR was decreased in Doc2α KOs, but not syt7 KOs, in response to the first pulse in the stimulus train. However, from the second action potential onwards, both KOs yielded reductions in AR as compared to WT, such that by the end of the train the fraction of AR was reduced by 53% and 50% in syt7 and Doc2α KO neurons, respectively (Fig. 3A-C; see also (*26*)).

One potential source of the observed phenotype in syt7 KO during the train is variability among synapses. That is, the boutons that respond to the second pulse onward may have different release properties. To test such a possibility, we analyzed the distribution of the iGluSnFR signals from 923 boutons. We did not observe spatial segregation of AR during the first two responses (see Fig. S3 for further analysis and details). Thus, the differences in AR between the first and second responses are not due to differences regarding which boutons responded during the first and second stimuli. Together, these data suggest that both Doc2α and syt7 contribute to AR from the second pulse onward during the train.

Next, we extended the train stimulation experiments to hippocampal slices, via patch clamp recordings (Fig. 4A), and observed the same trends that were obtained using iGluSnFR in cultured neurons (Fig. 3). Namely, peak amplitudes (synchronous release) depressed more slowly in Doc2α KO, and syt7 KO neurons had faster and more profound synaptic depression during the train, as compared to WT (Fig. 4B). Interestingly, loss of syt7 caused more severe synaptic depression than EGTA-AM. To estimate the extent of AR in these electrophysiological experiments, we calculated the tonic charge transfer, as previously described (Otsu et al., 2004, Yao et al., 2011), using the 20 Hz stimulation data. This approach revealed that syt7 and Doc2α KO neurons both exhibited 65% reductions in the tonic charge transfer component, similar to the EGTA-AM treatment condition (74%) (Fig. 4C). These data are all consistent with both Ca^{2+} binding proteins, Doc2α and syt7, playing essential roles in AR driven by residual Ca^{2+} (8, 16).

Doc2α mediates asynchronous fusion, while syt7 docks vesicles

Why is Doc2α essential for AR after single and multiple stimuli, while syt7 is only required starting with a second action potential? And why is short-term plasticity so catastrophically disrupted in syt7 KOs? Recent studies have proposed that synaptic vesicles rapidly transition from undocked to docked states during activity, and that this could, in principle, provide a common basis for AR, synaptic facilitation, and resistance to synaptic depression (34–40). In this

model, after Ca^{2+} influx, initially undocked and release-incompetent vesicles can dock and fuse ('two-step' release: (35, 41), resulting in AR, or dock and then fuse after another action potential, leading to facilitation and resistance to depression (34, 36). Consistent with this notion, we previously found that vesicles can dock within 15 ms of an action potential to replenish vacated release sites (23). Importantly, like AR and facilitation, this 'transient docking' is blocked by EGTA-AM. Thus, our imaging and electrophysiology findings could be explained by these two Ca^{2+} sensors playing distinct roles in docking and fusion, with Doc2α triggering AR, while syt7 mediates transient docking.

To test this hypothesis, we performed zap-and-freeze electron microscopy experiments (23). This approach allows us to measure synchronous and asynchronous vesicle fusion, as well as depletion and replenishment of docked vesicles, in the same experiment. Vesicles that appear to be in contact with the plasma membrane are considered docked. Unstimulated syt7 KO and Doc2α KO synapses appeared qualitatively normal (see Fig. 5A-D, 6A-D, and S5 for example micrographs). Knocking out either protein did not affect the number of docked vesicles at rest (Fig. 6D-E) nor the number and distribution of synaptic vesicles within 100 nm of the plasma membrane at the active zone (Fig. S6D). Therefore, the physiological defects in syt7 and Doc2α synapses cannot be accounted for by any ultrastructural phenotypes at rest.

We then assessed synaptic vesicle exocytosis by quantifying the appearance of exocytic pits following a single action potential (1 ms, 1.2 mM external Ca^{2+}, 37 ºC) and freezing the neurons at 5, 11, and 14 ms after the action potential. These time points capture synchronous fusion, asynchronous fusion, and transient docking, respectively (23, 42). Consistent with our previous findings (23, 42), in WT controls exocytic pits peaked at 5 ms after an action potential, declined to less than half of this peak at 11 ms, then further declined to baseline by 14 ms (Fig. 5E,F; pits in the active zone per synaptic profile: syt7 WT: no stim: 0.03 pits; 5 ms; 0.22 pits; 11 ms: 0.13 pits; 14 ms: 0.04 pits; Doc2α WT: no stim: 0.021 pits; 5 ms: 0.35 pits; 11 ms: 0.08 pits; 14 ms: 0.04 pits. See Fig. S6A for active zone sizes from each condition and Fig. S6B for pit data normalized to the size of active zones; see Supplementary Table 1 for full descriptive statistics and test statistics). In syt7 KOs, this sequence was unchanged: the number of pits at each time point in the KO was not different from the corresponding WT control (pits per synaptic profile: syt7 KO: no stim: 0.04 pits; 5 ms: 0.28 pits; 11 ms: 0.14 pits; 14 ms: 0.06 pits; $P > 0.9$ for each compared to the corresponding syt7 WT time point). By contrast, in Doc2α KO synapses, the number of pits at 5 ms was unchanged, but pits at 11 ms were almost completely abolished (pits per synaptic profile: Doc2α KO: no stim: 0.02 pits; 5 ms: 0.32 pits; 11 ms: 0.03 pits; 14 ms: 0.01 pits; $P = 0.04$ between WT and KO 11 ms, $P = 0.02$ between WT no stim and 11 ms, $P > 0.9$ between KO no stim and 11 ms). This phenotype mirrors the effect of EGTA-AM we previously reported (23), consistent with Doc2α being essential for residual Ca^{2+}-dependent AR. In sum, we obtained the same result from three different techniques (iGluSnFR imaging, patch-clamp electrophysiology, and zap-and-freeze electron microscopy): after a single action potential, Doc2α accounts for 54-67% of AR at hippocampal excitatory synapses, whereas deleting syt7 has no effect.

Is syt7 required for activity-dependent transient docking of synaptic vesicles? To test this possibility, we quantified all vesicles within 100 nm of the plasma membrane at the active zone. The distribution of undocked vesicles did not detectably change in any of the genotypes, nor at any of the time points after stimulation (Fig. S6D). WT controls showed rapid depletion and replenishment of docked vesicles after an action potential, as previously reported (Kusick et al., 2020; Fig. 6E,F.). At 5 and 11 ms, there were ~40% fewer docked vesicles than in the no-stim controls, then at 14 ms docked vesicles returned to baseline (Fig. 6E,F; docked vesicles per synaptic profile: syt7 WT: no stim: 2.19; 5 ms; 1.52; 11 ms: 1.36; 14 ms: 1.93; Doc2α WT: no stim: 1.90; 5 ms: 0.91; 11 ms: 1.00; 14 ms: 1.62. See Fig. S6A for active zone sizes from each condition and Fig. S6C for docked vesicle data normalized to the size of active zones; see Supplementary Table 2 for full descriptive statistics and test statistics). In syt7 KO, consistent with our previous data (26), there were ~25% fewer docked vesicles than in WT controls at 5 ms and 11 ms. At 14 ms, docked vesicles completely failed to recover in syt7 KO, remaining at less than half of the no-stim control (docked vesicles per synaptic profile: syt7 KO: no stim: 2.12; 5 ms: 1.07; 11 ms: 1.07; 14 ms: 1.09; $P < 0.0001$ between WT and KO at 14 ms, $P = 0.001$ at 5 ms between WT and KO, $P = 0.16$ at 5 ms between WT and KO). These data indicate that syt7 is absolutely required for transient docking of synaptic vesicles.
In Doc2α KO neurons, by contrast, we observed normal docked vesicle depletion and faster recovery (Fig. 6F). The number of docked vesicles was 40% greater in the KO than in the WT at 11 ms, about halfway towards full recovery to baseline (docked vesicles per synaptic profile: Doc2α KO: no stim: 1.85; 5 ms; 1.11; 11 ms: 1.40; 14 ms: 1.63; $P < 0.0001$ between WT and KO at 11 ms, $P < 0.0001$ between 11 ms and no stim in the KO). This is consistent with the idea that attenuation of AR spares some vesicles for ongoing synchronous release (8, 31), which could in part explain the slower train depression in Doc2α KOs (Fig. 3 and 4, though see **Model for sequential action of syt7 and Doc2α during asynchronous release** below for an alternate explanation for the apparent competition between AR and synchronous release). We conclude that transient docking completely fails in the absence of syt7, while Doc2α is dispensable for docked vesicle recovery. Taken together with our data on exocytosis, these results suggest that syt7 supports synchronous and asynchronous release after multiple stimuli by triggering transient docking, while Doc2α is the Ca^{2+} sensor for asynchronous fusion itself.

Model for sequential action of syt7 and Doc2α during asynchronous release

To further test the idea that syt7 and Doc2α act sequentially to support and drive AR, respectively, we constructed a model in which syt7 catalyzes vesicle docking and Doc2α and syt1 promote vesicle fusion by lowering the energy barriers for these reactions upon binding Ca^{2+} (see Fig. 7A for simplified scheme, and Fig. S7 for full reaction scheme). Because docking (unlike fusion) is reversible, the energy barrier height also determines undocking. In other words, syt7 essentially functions as a docking catalyst (43). Since they are both present on the plasma membrane (26, 44–46), syt7 and Doc2α were assumed to be part of the release site and thus bind Ca^{2+} irrespective of whether the site is occupied by a vesicle (see methods). In this way, the

release site (syt7 and Doc2α) maintains its Ca^{2+}-bound state independent of whether synaptic vesicles tether, dock, or fuse. This is highly relevant for Ca^{2+} sensors with high affinity but slow binding kinetics, like syt7 and Doc2α (8–10) and distinguishes them from the vesicular sensor syt1, which is unlikely to bind Ca^{2+} on undocked SVs (47, 48); this notion is included in our model. In the model, syt1 and Doc2α promoted transmitter release by lowering the energy barrier for vesicle fusion (following the dual-sensor model proposed by Sun et al., 2007 and Kobbersmed et al., 2020), and a direct competition between syt1 and Doc2α for Ca^{2+}-binding was assumed (i.e. the sensors need to bind a common resource to accelerate fusion, as suggested in (8, 14; see methods). The affinity of syt1 and syt7 as well as the Ca^{2+}-binding rate of syt1 and its effect on the energy barrier were estimated from the literature (see Supplementary Table 3). For simplicity, Doc2α was assumed to have the same Ca^{2+}-binding dynamics as syt7. The remaining reaction rates and the effect syt7 and Doc2α exert on the energy barriers were manually adjusted to obtain good qualitative correspondence to the experimental data presented (see Methods, Supplementary Table 3 and Fig. S8), but note that this solution is not unique (as indicated by parameter space evaluation, Fig. S9).

With these parameters and assumptions, we tested the sequential action of syt7 and Doc2α during the stimulus train. We used estimated Ca^{2+} transients resulting from 20 Hz AP trains to drive our model (Fig. 7B) and monitored Ca^{2+}-binding to Doc2α, syt7 and syt1, the number of docked vesicles, the peak rate of synchronous release, and the magnitude of asynchronous release. Our simulations indicate that all three sensors reach maximum Ca^{2+}-activation at a similar time (Fig. 7C) despite slower Ca^{2+}-binding rates of syt7 and Doc2α compared to syt1. However, syt1's low Ca^{2+} affinity but fast binding kinetics ensure that its Ca^{2+} association closely follows the shape of the Ca^{2+}-transient itself (Fig. 7C). Accordingly, the activation of syt1 by Ca^{2+} dominated the initial synchronous release immediately after the first AP and closely followed the predicted peak release rates. This synchronous component was not visibly dependent on Doc2α, assuming that Doc2α has a ~40% lower contribution to overcoming the fusion barrier than syt1 upon Ca^{2+} binding (Fig. 7G, Fig. S8). By contrast, AR in response to a single AP strongly depended on the delayed and sustained activation of Doc2α (Fig. 7C and F). Although Doc2α and syt7 were assumed to have a similar Ca^{2+} binding dynamics, syt7 did not contribute noticeably to the first AP response (Fig. 7F and G) due to its assigned role in docking. These results from the first action potential during the train stimulation are consistent with the functional experiments (Fig. 3 and Fig. 4).

During the stimulus train, synchronous release gradually decreased, while AR showed the opposite. Our simulations indicated that this phenomenon is likely due to the competition between Ca^{2+}-bound syt1 and Doc2α for a common recourse to elicit their effect on the fusion barrier (Fig. 7C). This result not only depended on Doc2α's higher Ca^{2+} affinity, but also on its sustained and persistent activation at release sites where vesicles had previously fused (data not shown). Removal of Doc2α from the model showed less depression of synchronous release and reduced asynchronous release (Compare Fig. 7E, G with Fig. 3D and 4B). These results are consistent with the experiments and suggest that, though less efficient in promoting fusion,

Doc2α-mediated fusion has increasingly more influence on synaptic transmission during extended AP trains.

As in the experiments, the relevance of syt7's ability to catalyze vesicle docking was revealed only from the second stimulus onward. Owing to its higher Ca^{2+} affinity and release site localization, syt7, like Doc2α, became increasingly activated over the duration of the stimulus train (Fig. 7C). Ca^{2+}-bound syt7 ensured a fast recovery of docked vesicles after depletion (independent of whether fusion depended on Doc2α and Syt1 or Syt1 alone, Fig. 7D). As observed experimentally in the syt7 KO (Fig. 6), removal of this catalytic function in the model resulted in very limited recovery of docked vesicles before the next stimulus (Fig. 7D). Because both synchronous and asynchronous release under prolonged stimulation depend on replenishment of vesicles, removal of syt7 from the model resulted in reduction of both release modes during the AP train (Fig. 7E, G), consistent with the syt7 KO data (Fig. 3 and 4). Thus, there is a good qualitative correspondence of our models to the experimental data.

Epistasis experiments indicate that syt7 and Doc2α act sequentially

The sequential model predicts that syt7 works upstream of Doc2α for asynchronous release. If syt7 and Doc2α act as parallel Ca^{2+} sensors triggering AR directly, rather than in sequence through transient docking (syt7) and fusion (Doc2α), the DKO would be expected to eliminate or reduce the remaining AR from either of the single knockouts. To test this prediction, we performed an epistasis experiment using double knockout (DKO) mice. For these experiments we conducted hippocampal slice electrophysiology. We first applied single action potentials and observed that loss of both proteins was not additive: the reduction in slow EPSC charge was identical in Doc2α neurons compared to Doc2α/syt7 DKOs (Fig. 8A,B); again, EGTA-AM served as a control. This was the expected result, as syt7 does not regulate release triggered by single stimuli. We then applied train stimulation (Fig. 8C) and again quantified the tonic charge transfer component as a measure of AR (Fig. 8D). Importantly, no differences were observed between the Doc2α KO and the Doc2α/syt7 DKO condition. In DKOs, short-term plasticity of synchronous release early in the train was similar to EGTA-treated neurons, with abolished paired-pulse facilitation but not the enhanced depression seen in syt7 KOs (Fig. S11). This is consistent with the idea that disrupting asynchronous release, but not transient docking, produces the slower depression in Doc2α KOs, while disrupting transient docking, but not asynchronous release, causes the faster depression in syt7 KOs. Disrupting both, with EGTA or DKO, balances out to a similar rate of depression as the WT. However, late in the train amplitudes decayed to the same lower level as syt7 KOs, indicating a specific role for syt7 in limiting steady-state depression (Fig. S7). Together, these findings strongly support a sequential model for the action of syt7 and Doc2α (illustrated in Fig. S12, as detailed below).

Consistent with the experimental data, removal of both proteins from the model resulted in less depression of synchronous release compared to the simulations lacking syt7 only (Fig. S10), because Ca^{2+}-bound syt1 gains more access to the fusion machinery in this phase when not competing with Doc2a. This result matches the experimental observations (Fig. S11). At the

same time, the model predicted reduced asynchronous release after 10 action potentials in this situation (Fig. S10C) while experimental analysis detected no difference in the cumulative charge of DKOs compared to Doc2α KOs after 50 action potentials (Fig. 8D). This could be due to the clamping function of syt1 exerts on AR, which is not included in this simple model (see Discussion). Nonetheless, our modelling study confirms that a sequential action of syt7 and Doc2α in the Ca^{2+}-dependent docking and fusion of synaptic vesicles, respectively, can explain phenotypes observed in Doc2α KO, syt7 KO and partially that of DKO neurons.

Discussion

Resolving the asynchronous release Ca^{2+} sensor controversy

Both Doc2α (8) and syt7 (16) have been implicated in AR, but conflicting results over the years led to an unresolved debate - which sensor mediates AR? Several factors may have contributed to these inconsistent results, including stimulation frequency, the type of synapse under study, and method used to measure release. To minimize the effects from these different factors, we conducted a side-by-side comparison of Doc2α and syt7 KO neurons, using direct optical measurements of glutamate release, patch clamp electrophysiology, and ultrastructural characterization of millisecond-by-millisecond vesicle dynamics from cultured mouse hippocampal neurons. These experiments show that Doc2α drives significant levels of AR after a single action potential. In sharp contrast, knocking out syt7 has a negligible effect on this mode of release in response to a single action potential. Remarkably, during a stimulus train, both Doc2α and syt7 are equally important for AR. These results resolve some of the inconsistencies in the literature. First, Doc2α is a Ca^{2+} sensor for AR both after a single stimulus, and also during the train in both cultured hippocampal neurons and Schaffer collaterals. Second, syt7 contributes to AR, but its role is only apparent from the second action potential onward. Thus, at least in excitatory mouse hippocampal synapses, these sensors both contribute to AR. However, it is still likely that which sensor(s) are required depends on synapse type, since Doc2α played no apparent role in transmission at Purkinje cell to deep cerebellar nuclei synapses (13). This, along with our finding that syt7/Doc2α DKOs still had remaining AR, raises the possibility that there are other unidentified calcium sensors for AR. Thus, further work should explore the diversity of synaptic Ca^{2+} sensors and how they contribute to heterogeneity in synaptic transmission throughout the brain.

Physiological relevance of rapid activity-dependent docking triggered by syt7

How syt7 contributes to three separate phenomena, paired-pulse facilitation, AR, and resistance to synaptic depression, is a major question in the field (15, 26, 32, 50). Our data suggest that syt7 drives activity-dependent transient docking to support all three processes. In the case of paired-pulse facilitation it feeds docked vesicles to syt1 to enhance release in response to the second stimulus; it likely functions in the same manner to reduce synaptic depression during train stimulation. In the case of AR, it feeds vesicles to Doc2α, which then directly triggers this slow

mode of transmission. This is consistent with the recent proposal that activity-dependent docking underlies both short-term plasticity and AR (34–37, 40), though see (51) for a correlation between short-term plasticity and AR with a different proposed mechanism.

Three pieces of data reported here support this notion. First and foremost, transient docking, which appears to mirror the time course of paired-pulse facilitation (23), is completely blocked in syt7 KO hippocampal neurons. Consequently, these synapses do not facilitate, instead depressing quickly and profoundly, suggesting that syt7-mediated docking is at least in part necessary for facilitation. Second, despite release probability not changing, docked vesicles are more severely depleted (~33% compared to wild type at 5 ms after an action potential) in syt7 KO both after single action potentials (this study) and high-frequency trains (26). This implies that vesicles are normally recruited by syt7 to the active zone continuously during the first 15 ms after stimulation in WT synapses. Third, in the absence of the asynchronous Ca^{2+} sensor Doc2α, the recovery of docked vesicles is significantly faster, nearly returning to baseline by 11 ms, suggesting that some vesicles docked by syt7 are fused by Doc2α. Although we cannot rule out the possibility that Doc2α works by docking and then fusing vesicles that are initially undocked, slowed train depression of synchronous release and faster docked vesicle replenishment in Doc2α KO suggests vesicles are still being recruited in the absence of Doc2α, but do not fuse asynchronously. Thus, these data show that syt7-mediated docking contributes to both AR and short-term plasticity. We tested our model for the sequential action of syt7 and Doc2α by conducting an epistasis experiment using DKO mice. Disruption of syt7 did not exacerbate the loss of AR in Doc2α KOs either after single stimuli or train stimulation. These findings are consistent with the idea that syt7 functions upstream of Doc2 in a common pathway, with the upstream step (transient docking) required only during sustained activity (summarized in the model shown in Fig. S8).

A sequential model of syt7 and Doc2 in transmitter release

We showed that a model in which syt7 acts upstream of Doc2α by catalyzing synaptic vesicle docking is qualitatively consistent with multiple experimental observations reported here. Both experiment and model showed that (1) syt7-mediated docking promotes synchronous and asynchronous release from the second stimulus onwards, and that (2) Doc2α promotes asynchronous release at the costs of synchronous synaptic transmission. This correspondence could only be observed when syt7 and Doc2α are located at release-sites, allowing their uninterrupted activation during prolonged stimulation. This constitutes a major difference from the vesicular sensor syt1, which can only undergo significant activation when synaptic vesicles are docked. Furthermore, competition between syt1 and Doc2α was needed to generate the reduced depression observed in Doc2αKO neurons. This is because, unlike in the ultrastructural experiments, removing Doc2α from the model had no effect the speed of docked vesicle recovery. Apparent competition between AR and synchronous release over a limited supply of docked vesicles (as proposed by (31) and (8), and suggested by the EM here), and direct competition between the sensors for the release machinery (as suggested by the model), could

both explain why Doc2α KOs exhibit slower depression of synchronous release. The direct competition between sensors could indicate a need to bind to common, limited number of "slots" at the release site (e.g. SNARE complexes or lipid clusters; (8, 14, 52–56)). Our model describes the association to these slots implicitly by lumping it together with Ca^{2+} binding and synaptic vesicle fusion. This also means that our model can only account for Ca^{2+}-dependent functions. Recent analysis, however, indicates that syt1 pre-associates to these slots at resting Ca^{2+}-concentrations, which would limit access for other sensors (56). This arrangement would account for the reported clamping syt1 exerts on spontaneous transmission (57–59) and asynchronous release (60, 61).

In our model, we implemented syt7 as a catalyst for synaptic vesicle docking, meaning that Ca^{2+}-bound syt7 lowers the energy barrier for docking, like Doc2α and syt1 do for fusion. This makes comparison of the three proteins easier. Moreover, it means that the number of docked vesicles at rest is independent of the presence of syt7, accounting for the observation that steady-state docking is normal in syt7KO neurons (18, 19). The disadvantage of this implementation is that the catalytic action does not allow an overshoot in the number of docked vesicles. While that is consistent with the EM data presented here, this is at odds with the established role of syt7 in facilitation (19, 33), as facilitation has been proposed to depend on an increase in the number of docked/primed vesicles (34, 40, 62). This could indicate that facilitation might rely on a post-docking function of syt7. Since the synaptic responses studied here only facilitated slightly (which could be accounted by factors other than calcium sensing, such as action potential broadening; (63)), we restricted the model to the catalytic function of syt7 in synaptic vesicle docking. As in other secretory cell types (64), syt7 is indeed able to act as a direct Ca^{2+} sensor for exocytosis. Thus, there will be conditions the model is currently unable to explain. Nonetheless, while the model is a simplification, the sequential action of syt7 and Doc2α can explain the role of these proteins in asynchronous release in mouse hippocampal synapses.

Methods

All animal care was performed according to the National Institutes of Health guidelines for animal research with approval from the Animal Care and Use Committees at the Johns Hopkins University School of Medicine and the University of Wisconsin, Madison (Assurance Number: A3368-01). Both male and female syt7^{KO}, Doc2α^{KO}, and WT littermates were used.

Mouse lines used for this study were as follows:
- C57BL/6-*Syt7*^{tm1Nan} (28)
- C57BL/6-*DOC2*α^{em1Smoc} (27)
- C57BL/6-*DOC2*α^{em1Smoc};C57BL/6-*Syt7*^{tm1Nan}

Double knockouts were maintained as homozygous null. Single knockout lines were maintained as heterozygotes, except for double knockout electron microscopy experiments, in which *DOC2*α$^{+/+}$ mice were used as the wild-type control.

Neuronal cell culture

For single-knockout experiments, Doc2α and syt7 KO mice were maintained as heterozygotes, so that littermate controls could be used. These mice were bred, and postnatal day 0-1 pups were genotyped, with homozygotes for the null allele (-/-) and the wild-type allele (+/+) being used for culture. For double knockout experiments, mice were maintained as homozygotes, with *Doc2α*$^{+/+}$ used as the wild-type control. For iGluSnFR experiments, WT and KO hippocampal neurons were grown in mass culture for 14 DIV. In brief, hippocampi were dissected from mouse brains and digested for 25 min at 37 °C in 0.25% trypsin-EDTA (Corning). After mechanical dissociation, hippocampal neurons were plated on 12 mm glass coverslips pretreated with poly-D-lysine (Thermofisher). Neurons were cultured in Neurobasal A (GIBCO) based media with B27 (2%, Thermofisher) and GlutaMAX (2 mM, GIBCO) at 37 °C with 5% CO2.

For high-pressure freezing and electron microscopy, cell cultures were prepared on 6-mm sapphire disks atop a feeder layer of astrocytes, as previously described (23). Astrocytes were harvested from cortices with the treatment of trypsin (0.05%) for 20 min at 37 °C, followed by trituration and seeding on T-75 flasks containing DMEM supplemented with 10% FBS and 0.2% penicillin-streptomycin. After 2 weeks, astrocytes were plated on 6-mm sapphire disks (Technotrade Inc) coated with poly-D-lysine (1 mg/ml), collagen (0.6 mg/ml) and 17 mM acetic acid at a density of 13 x 103 cells/cm^2. Genotyping was performed either 1) after hippocampal dissection, using cortices lysed with 10 mM Tris-HCL pH8.0 and 100 mM NaCl in the presence of 50 µg proteinase K, with hippocampi either left in Neurobasal A at 37 °C before switching to papain after or left in dissection medium (1% penicillin-streptomycin, 1 mM pyruvate, 10 mM HEPES, 3 mM glucose in HBSS) at 4 °C, or 2) using tail clips (alkaline lysis; Truett et al., 2000) of live mice, which were then sacrificed and dissected after genotyping was finished. We note that leaving the neurons in dissection medium at 4 °C results in more consistent cell health than Neurobasal A at 37 °C, particularly when hippocampi are left for several hours while genotyping is performed. Hippocampi were dissected under a microscope and digested with 1) papain (0.5 mg/ml) and DNase (0.01%) in the dissection medium for 25 min at 37 °C with gentle perturbation every 5 min or 2) papain (0.5 mg/mL) in Neurobasal A with 200 rpm shaking. After trituration, neurons were seeded onto astrocyte feeder layers at a density of 20 x 10^3 cells/cm^2 (75,000 per well) and cultured in Neurobasal A with 2% B27 and 2 mM at 37 °C with 5% CO2. Before use, sapphire disks were carbon-coated with a "4" to indicate the side that cells are cultured on. The health of the cells, as indicated by de-adhered processes, floating dead cells, and excessive clumping of cell bodies, was assessed immediately before experiments.

Plasmids

-pF(UG) CamKII sf iGluSnFR A184V (29); Addgene #158769

-pF(UG) CamKII sf iGluSnFR S72A (26)

Lentivirus production and use

For viral transduction, the original (24, 29) and low-affinity glutamate S72A were used (25, 26). iGluSnFRs were subcloned into a FUGW transfer plasmid (29). Lentiviral particles were generated as previously described (26, 29) by co-transfecting the transfer, packaging, and helper (pCD/NL-BH*ΔΔΔ and VSV-G encoding pLTR-G) plasmids into HEK 293/T cells. Lentivirus was collected from the media 48–72 h after transfection and concentrated by ultracentrifugation. Viruses were titrated and then used to infect neurons on DIV 3-5.

iGluSnFR imaging and quantification

iGluSnFR fluorescence intensity changes were recorded and analyzed as previously described (26, 29), with

slight adjustments to imaging time and binning. To measure iGluSnFR signals in response to a single stimulus, the medium-affinity iGluSnFR (A184V) was used in Fig. 1A-D and S1. For train stimulation, the low-affinity iGluSnFR sensor (S72A) was used because it more effectively resolved individual responses from high-frequency stimulation due to its faster decay time (26). Imaging was performed in media (305 mOsm) comprising (in mM): 128 NaCl, 5 KCl, 2 $CaCl_2$, 1 $MgCl_2$, 30 D-glucose, and 25 HEPES, pH 7.3, with D-AP5 (50 µM) (Abcam; ab120003), CNQX (20 µM) (Abcam; ab120044), Picrotoxin (100 µM) (Tocris; 1128) added to prevent recurrent excitation. Single image planes were acquired (2x2 binning) with 10 ms exposure (100 Hz) using 488 nm excitation and 520 emission. Single planes were selected so that the highest amount of iGluSnFR expressing dendrite arbor was in focus. Laser intensity was set so that the amplitude of iGluSnFR peaks ($\Delta F/F0$) from a 0.5 Hz field stimulus did not change over the course of at least 20 s (photobleaching error). For single stimuli imaging, 200 frames (10 ms exposure/2 s total) were collected and a single field stimulus was triggered at 500 ms after the initial frame. For train stimuli imaging, 50 stimuli at 10 Hz (5 s) or 20 Hz (2.5 sec) were applied via field stimulation, and 500 or 750 frames, each with a 10 ms exposure time, were collected. Single and train (10 Hz) stimuli (1 ms square pulses) were triggered by a Grass SD9 stimulator through platinum parallel wires attached to a field stimulation chamber (Warner Instruments; RC-49MFSH). Voltage for field stimulus was set to the lowest voltage that reliably produced presynaptic Ca^{2+} transients in most (>95%) presynaptic boutons (5-30 V). All iGluSnFR imaging experiments were performed at 33–34°C. Temperature and humidity were controlled during experiments by a Tokai incubation controller and chamber. Glutamate release signals were defined as fluorescence intensity changes that > five- times the standard deviation of the noise (Fig. S1C). For all iGluSnFR experiments, we initially recorded 500 ms as the baseline; the mean intensity was defined as F0. iGluSnFR fluorescence amplitude changes are reported as $\Delta F/F0$. Throughout this study, we term regions of interest as boutons because these regions were defined as yielding at least one iGluSnFR response during the first three stimuli of a 10 Hz train. iGluSnFR data were analyzed using a custom ImageJ plugin (29) as follows: the macro begins by subtracting the average projection intensity (the pre-stimulation baseline) from a maximum intensity projection (the largest intensity from the entire image series). The result was duplicated, and the mean was filtered by an area of a radius of 10 pixels. The copied image is converted to a 32-bit image for subsequent calculations. The original duplicated and filtered images are subtracted, creating a new image ("Result"). Thresholding is applied to the "Result" image, converting it to a binary image. Watershed segmentation was then used to separate touching objects. The results were copied and imported into Axograph X 1.7.2 (Axograph Scientific), where traces were normalized, and background subtracted using pre-stimulus data. All iGluSnFR imaging and analysis was performed blind to genotype.

Brain slice preparation

Acute hippocampal slices were prepared from mice aged between P30 and P60. Animals were anesthetized using isoflurane and then rapidly decapitated. Brains were quickly removed and placed into ice-cold NMDG-HEPES artificial cerebral spinal fluid (aCSF; 300–310 mOsm) comprising (in mM): 92 N-Methyl-D-glucamine (NMDG), 2.5 KCl, 1.25 NaH_2PO_4, 30 $NaHCO_3$,
25 glucose, 2 thiourea, 5 Na-ascorbate, 3 Na-pyruvate, 0.5 $CaCl_2$, and 10 $MgSO_4$, and 20 HEPES, pH7.3. This solution was continuously bubbled with 95% O_2 and 5% CO_2. Three hundred µm thick coronal brain sections containing the hippocampal region were cut using a vibratome (Leica VT1200, Leica, Germany). To avoid any potential recurrent excitation, a sharp cut was made between CA3 and CA1. Slices were placed in a chamber and allowed to recover in 150 ml artificial cerebral spinal fluid at 34 °C for 25 min. Sodium (2 M stock in artificial cerebral spinal fluid) was added back at the following time intervals: 0 min (250 µl), 5 min (250 µl), 10 min (500 µl), 15 min (1 ml), and 20 min (2 ml) during the 25 min recovery incubation. Slices were then gently placed into another chamber containing aCSF, but with 92 mM NMDG replaced with 92 mM

NaCl, at room temperature (at least 1 hour) before being transferred to the recording chamber.

Electrophysiological recordings in acute hippocampal slices

Whole-cell voltage-clamp recordings were performed under an upright microscope (BX51WI, Olympus, Melville, NY) equipped with a water-immersion objective (LUMPlanFL N 40x/0.8 W; Olympus, Melville, NY). Hippocampal slices were continuously perfused (2 ml/min) with carbogen-saturated, modified aCSF (in mM: 125 NaCl, 25 NaHCO3, 25 glucose, 2.5 KCl, 2 CaCl2, 1.25 NaH2PO4, and 1 MgCl2, adjusted to 300-310mOsm). For perfusion, aCSF was heated to 34°C using a Single Channel Temperature Controller (TC-324C, Warner Instruments, Holliston, MA). Recording pipettes were prepared from borosilicate glass (1.5 mm diameter glass capillary, Sutter Instrument, Novato, CA) using a two-step puller (PP-830, Narishige, Japan), and were polished using an MF-830 micro forge (Narishige, Japan) immediately prior to use. Pipette position was controlled using an MP-285 motorized micromanipulator (Sutter Instrument, Novato, CA); the resistances were typically 4-6 MΩ when filled with recording solution consisting of (in mM): 135 K-gluconate 5 KCl, 10 HEPES, 1 EGTA, 6 Na_2 phosphocreatine, 0.3 Na_3GTP and 2 MgATP. To chelate residual Ca^{2+}, EGTA-AM (Millipore, Burlington, Massachusetts) was added to the bath at a final concentration of 25 µM for 30 minutes; neurons were then allowed to recover for another 20 minutes before being placed in the recording chamber. Neurons in the CA1 region were visualized using a Retiga electro CCD camera (ELEDYNE PHOTOMETRICS, Tucson, AZ). Patched neurons were held at −70 mV, with access resistance (Ra) less than 20 MΩ throughout the recordings. A concentric bipolar electrode (FHC, 125/50 µm extended tip) was placed in the stratum radiatum (Schaffer collateral fiber) ~300-500 µm away from the recording pipette (note that this large bore diameter is responsible for the large currents in our recordings). Stimulation strength was selected by starting at 0.5-1.5 mA, steadily increasing stimulation strength and adjusting electrode position until stable currents from 1 Hz test stimuli were achieved. EPSCs were pharmacologically isolated by bath application of 50 µM D-APV and 20 µM bicuculine. QX-314 chloride (5 mM) was in the pipette solution for evoked recordings. All data were collected in voltage-clamp mode using a Multiclamp 700B patch-clamp amplifier (Molecular Devices, San Jose, CA, USA) and a Digidata 1500B (Axon Digidata 1500B, Molecular Devices). Asynchronous release during 20 Hz stimulation (i.e., tonic charge transfer during the train) was quantified as illustrated in Fig. 4A. This was done by calculating the area between the baseline, before the first stimulus, and the tail current values, which were measured 1 ms before each stimulus in the train (8, 31). All recordings and analysis were performed blind to genotype.

High-pressure freezing and freeze substitution

Cells cultured on sapphire disks were frozen using an EM ICE high-pressure freezer (Leica Microsystems), exactly as previously described (23). The freezing apparatus was assembled on a table heated to 37 °C in a climate control box, with all solutions pre-warmed (37 ºC). Sapphire disks with neurons were carefully transferred from the culture medium to a small culture dish containing physiological saline solution (140 mM NaCl, 2.4 mM KCl, 10 mM HEPES, 10 mM glucose; pH adjusted to 7.3 with NaOH, 300 mOsm). NBQX (3 µM; Tocris) and bicuculline (30 µM; Tocris) were added to the physiological saline solution to block recurrent synaptic activity.

$CaCl_2$ and $MgCl_2$ concentrations were 1.2 mM and 3.8 mM, respectively. After freezing, samples were transferred under liquid nitrogen to an EM AFS2 freeze substitution system at -90 °C (Leica Microsystems). Using pre-cooled tweezers, samples were quickly transferred to anhydrous acetone at -90 °C. After disassembling the freezing apparatus, sapphire disks with cells were quickly moved to cryovials containing freeze substitution solutions. For the first two of three Syt7 knockout freezes, freeze substitution was performed exactly as previously described in (23): solutions were 1% glutaraldehyde, 1% osmium tetroxide, and 1% water in anhydrous acetone, which had been stored under liquid nitrogen then moved to the AFS2 immediately before use. The freeze substitution program was as follows: −90 °C for 6-10 hr (adjusted so substitution would finish in the morning), 5 °C h^{-1} to −20 °C, 12 h at -20 °C, and 10 °C h^{-1} to 20 °C. For all other experiments, we used a different freeze substitution protocol that yields more consistent, high-contrast morphology, as described in (26): samples were first left in 0.1% tannic acid and 1% glutaraldehyde at -90 °C for ~36 hours, then washed 5x, once every 30 min, with acetone, and transferred to 2% osmium tetroxide, then run on the following program: 11 hr at −90 °C, 5 °C h^{-1} to -20 °C, -20 °C for 12 hr, 10 °C h^{-1} to -4 °C, then removed from the freeze substitution chamber and warmed at room temperature for ~15 min before washing. For this latter protocol, instead of cryovials, solutions and sapphires were stored in universal sample containers (Leica Microsystems)**,** covered in aclar film to prevent evaporation. Using these containers instead of cryovials makes all solution transfers, from fixation through infiltration and embedding, much faster and more convenient.

Infiltration, embedding, sectioning, and transmission electron microscopy

Infiltration, embedding, and sectioning were performed as previously described (23), except without en-bloc staining, which we found to not improve morphology. Samples in fixatives were washed three times, 10 min each, with anhydrous acetone, then left in 30% epon araldite (epon, 6.2 g; araldite, 4.4 g; DDSA, 12.2 g; and BDMA, 0.8 ml, diluted in acetone) for 3 h, then 70% epon araldite for 2 h, both with shaking. Samples were then transferred to caps of polyethylene BEEM capsules (EMS) and left in 90% epon araldite overnight at 4 °C. The next morning, samples were transferred to 100% epon araldite for 1 h, then again to 100% for 1 h, and finally transferred to 100% epon araldite and baked at 60 °C for 48 h.

For ultramicrotomy, 40-nm sections were cut. Sections on single-slot grids coated with 0.7% pioloform were stained with 2.5% uranyl acetate then imaged either at 120 kV on the 57,000x setting on a Thermo-Fisher Talos L120C equipped with a Ceta camera (pixel size = 244 pm; first replicate of the Doc2 experiment) or at 80 kV on the 100,000x setting on a Hitachi 7600 TEM equipped with an AMT XR50 camera run on AMT Capture v6 (pixel size = 560 pm, all other experiments). Samples were blinded before imaging. To further limit bias, synapses were found by bidirectional raster scanning along the section at the magnification at which images were taken, which makes it difficult to "pick" certain synapses, as a single synapse takes up most of this field of view. Synapses were identified by a vesicle-filled presynaptic bouton and a postsynaptic density. Postsynaptic densities are often subtle in our samples, but synaptic clefts

were also identifiable by 1) their characteristic width, 2) the apposed membranes following each other closely, and 3) vesicles near the presynaptic active zone. 125-150 micrographs per sample of anything that appeared to be a synapse were taken without close examination. All images were from different synapses (that is, images were never captured from different sections of the same synapse). Most of the time all images for a condition were taken from a single section, each of which typically contains hundreds of different boutons; when different sections were used, they were always at least 10 serial sections apart (400 nm in z) to ensure they didn't contain any of the same boutons.

Electron microscopy image analysis

EM image analysis was performed as previously described (23). All the images from a single experiment were randomized for analysis as a single pool. Only after this randomization were any images excluded from analysis, either because they appeared to not contain a bona fide synapse, or the morphology was too poor for reliable annotation. The plasma membrane, the active zone, docked synaptic vesicles, and all synaptic vesicles within ~100 nm of the active zone were annotated in ImageJ using SynapsEM plugins (66) [https://github.com/shigekiwatanabe/SynapsEM copy archived at swh:1:rev:11a6227cd5951bf5e077cb9b3220553b506eadbe]. The active zone was identified as the region of the presynaptic PM with the features described above for identifying a synapse. Docked vesicles were identified by their membrane appearing to be in contact with the PM at the active zone (0 nm from the PM); that is, there are no lighter pixels between the membranes. Vesicles that were not manually annotated as docked but were 0 nm away from the active zone PM were automatically counted as docked when segmentation was quantitated (see below) for data sets counting the number of docked vesicles. Likewise, vesicles annotated as docked were automatically placed in the 0 nm bin of vesicle distances from the PM. To minimize bias and error, and to maintain consistency, all image segmentation, still in the form of randomized files, was thoroughly checked and edited by a second member of the lab. Features were then quantitated using the SynapsEM (Watanabe et al., 2020) family of MATLAB (MathWorks) scripts (https://github.com/shigekiwatanabe/SynapsEM). Example electron micrographs shown were adjusted in brightness and contrast to different degrees (depending on the varying brightness and contrast of the raw images), rotated, and cropped in ImageJ before import into Adobe Illustrator.

Statistics

Statistical analysis was performed using GraphPad Prism 9 software. iGluSnFR and electrophysiology data were presented as mean ± standard error of the mean. Electron microscopy data were presented as mean and 95% confidence interval of the mean. For iGluSnFR and electrophysiology, data sets were tested for normality using the Anderson-Darling test and corresponding parametric or non-parametric hypothesis tests performed, as stated in the figure legends. Since electron microscopy pit and docked vesicle data are count data, following a

roughly binomial rather than normal distribution, means were used to graph the data (medians are not a useful representation of central tendency for count data, particularly low-frequency count data; for example, the median number of pits in all samples is 0 since exocytic pits are rare) and Games-Howell post-hoc test used, which does not assume a normal distribution.

Mathematical model

In the model we developed a release site can be in one of three states: empty, occupied with a tethered vesicle or occupied with a docked vesicle (for full scheme see Fig. S9). Only docked vesicles can fuse and their fusion rates depend on the number of Ca^{2+} ions bound to syt1 and Doc2α. Ca^{2+} binding to these Ca^{2+} sensors followed the reaction scheme as previously published by Kobbersmed et al., 2020, in which five Ca^{2+} ions per vesicle can bind to the first Ca^{2+} sensor for fusion (syt1 in our model), and two Ca^{2+} ions to the second Ca^{2+} sensor for fusion (Doc2α in our model). We adjusted the dual-sensor model such that no more than five Ca^{2+} ions can be bound in total to syt1 and Doc2α simultaneously. Ca^{2+} can bind to Doc2α at any of the release site states. Ca^{2+} binding to syt1 only occurs when vesicles are docked. Together the model is described by the following differential equations:

$$d\frac{E[0]}{dt} = -k_{tet}E[0] + k_{untet}T[0] + \sum_{i=0}^{5}(f(0,i)D[0,i]) + k_{2-}E[1] - 2Ca^{2+}\,k_{2+}E[0]$$

$$d\frac{E[1]}{dt} = -k_{tet}E[1] + k_{untet}T[1] + \sum_{i=0}^{5}(f(1,i)D[1,i]) + 2k_{2-}b_2E[2] + 2Ca^{2+}\,k_{2+}E[0] - (Ca^{2+}\,k_{2+} + k_{2-})E[1]$$

$$\frac{E[2]}{dt} = -k_{tet}E[2] + k_{untet}T[2] + \sum_{i=0}^{5}(f(2,i)D[2,i]) + Ca^{2+}\,k_{2+}E[1] - 2k_{2-}b_2\,E[2]$$

$$d\frac{T[0]}{dt} = k_{tet}E[0] - k_{untet}T[0] + \sum_{i=0}^{5}(undocking\ D[0,i]) - docking\ T[0] + k_{2-}T[1] - 2Ca^{2+}\,k_{2+}T[0]$$

$$d\frac{T[1]}{dt} = k_{tet}E[1] - k_{untet}T[1] + \sum_{i=0}^{5}(undocking\ D[1,i]) - docking\ T[1] + 2k_{2-}b_2\,T[2] + 2Ca^{2+}k_{2+}T[0] - (Ca^{2+}k_{2+} + k_{2-})T[1]$$

$$d\frac{T[2]}{dt} = k_{tet}E[2] - k_{untet}T[2] + \sum_{i=0}^{5}(undocking\ D[2,i]) - docking\ T[2] + Ca^{2+}\,k_{2+}T[1] - 2k_{2-}b_2T[2]$$

$$\begin{aligned} d\,\frac{D[d2,s1]}{dt} = {} & \mathbf{1}_{s1\geq 1}\ \max\big(0, 5-(d2+s1-1)\big)\ Ca^{2+}\,k_{1+}\,D[d2,s1-1] \\ & + \mathbf{1}_{s1<5}\,(s1+1)\,b_1^{s1}\,k_{1-}\,D[d2,s1+1] \\ & + \mathbf{1}_{d2\geq 1}\min\big(\max(0,2-\mathrm{d2}+1), \max\big(0,5-(d2+s1-1)\big)\big)\ Ca^{2+}\,k_{2+}\,D[d2-1,s1] \\ & + \mathbf{1}_{d2<2}\,(d2+1)\,b_2^{d2}\,k_{2-}\,D[d2+1,s1] \\ & + \mathbf{1}_{s1=0}\,docking\ T[d2] \\ & - \Big(\max\big(0,5-(d2+s1)\big)\ Ca^{2+}\,k_{1+} + s1\,b_{1-}^{s1}\,k_{1-} + \min\big(\max(0,2-d2), \max\big(0,5- \\ & (\mathrm{d2}+\mathrm{s2})\big)\Big)\ \mathrm{Ca}^{2+}\,\mathrm{k}_{2+} + d2\,b_2^{d2-1}\,k_{2-} + f(d2,s1) + undocking)\,D[d2,s1] \end{aligned}$$

$$\frac{dF}{dt} = f(d2, s1)\ D[d2, s1]$$

E(d2), T(d2), D(d2,s1) denote the Ca^{2+} binding state of the empty release site, tethered and docked vesicle respectively, with d2 the number of Ca^{2+} ions bound to Doc2α and s1 the number of Ca^{2+} ions bound to syt1. F indicates the fused vesicles and f is the fusion rate function:

$$f(d2, s1) = l_{+} f_1^{s1} f_2^{d2}$$

In the model docking and undocking rates are dependent on the number of Ca^{2+} ions bound to syt7. Binding of Ca^{2+} to syt7 follows the same scheme as Doc2α, and can be described by the following rate equations:

$$d\frac{S[0]}{dt} = k_{7-}\, S[1] - (2\ k_{7+} Ca^{2+}) S[0]$$
$$d\frac{S[1]}{dt} = 2\ Ca^{2+} k_{7+}\, S[0] + 2 b_7 k_{7-}\, S[2] - (\ k_{7+} Ca^{2+} + k_{7-}) S[1]$$
$$d\frac{S[2]}{dt} = Ca^{2+} k_{7+}\, S[1] - (2\ b_7\ k_{7-}) S[2]$$

Here, S(s7) denotes the proportion of syt7 with s7 number of Ca^{2+} ions bound. From these states the docking and undocking rates can be computed following:

$$docking = k_{docking} \sum_{s7=0}^{2} S[s7]\ f_7^{s7}$$
$$undocking = k_{undocking} \sum_{s7=0}^{2} S[s7]\ f_7^{s7}$$

To compute the steady state of the system, all reaction rates (from one state to another, except the Ca^{2+} binding states of syt7) were rewritten into an intensity matrix, Q, in which element i,j describes the rate from state i to state j. Steady state of these reactions was computed using the equation:

$$\pi e^{Qt}$$

With a vector of 24 zeros, and the first element set to total number of release sites in the model, and t equal to 1000. To reduce the dimensions Q, the steady state of syt7 was solved separately by setting the first state, S[0] to 1. Subsequently S[1] and S[2] were computed by:

$$S[1] = \frac{2Ca^{2+} k_{7+}}{k_{7-}}$$
$$S[2] = \frac{Ca^{2+} k_{7+}}{b_7 k_{7-}}$$

Next, S[0], S[1] and S[2] were divided by the sum of those three elements. The steady state of the system was computed for a resting Ca^{2+} concentration of 0.05 µM. With values as a starting point, the differential equations were solved in Matlab (2020b) using ode15s (MaxStep =

$1e^{-5}$,RelTol =$1e^{-5}$, AbsTol = $1e^{-5}$)and a Ca^{2+} transient corresponding to ten APs at 20Hz as input. The Ca^{2+}-transient for a single AP was generated using a normal distribution (mean=+1.5ms, sd=0.2ms), which was scaled to obtain the desired amplitude (supplementary table 3). To this Ca^{2+}-transient a residual signal was added, which followed an exponential decay (starting at +1.6ms from the start of each AP);

$$\mathbf{1}_{t\geq t0}Ae^{-\frac{(t0+t)}{tau}}$$

with, t0 the starting times of the residual Ca^{2+}-signal (+1.6 ms), tau the decay time constant and t time. For smoothening of the Ca^{2+}-transient, the exponentially decay function was multiplied with:

$$\frac{t-t0}{t-t0+km}$$

with km set to 0.1ms. To the entire Ca^{2+}-transient, a basal concentration of 0.05 µM was added.

The simulated cumulative number of fused vesicles was interpolated at a sampling rate of $50e^3$ Hz. From this release rates were computed by multiplying the difference between two time points with the sampling rate. The maximum release rate between stimulus onset (0ms) and the onset of the next stimulus (+50ms) was taken as the peak release rate of each stimulus. All release events occurring at +5ms from stimulus onset to the onset of the next stimulus (+50ms) were considered as asynchronous release events.

Parameters in the model were constraint to experimentally obtained values, if available. For a list of all model parameters see supplementary table 3. To simplify the model, we assumed that both syt7 and Doc2α have the same Ca^{2+}-binding dynamics, and that undocking and untethering rate constants were equal to the docking and tethering rate constants, respectively. The remaining free parameters, f_2, f_7, k_{tet}, $k_{docking}$, amplitude of Ca^{2+}-transient, amplitude of residual Ca^{2+} and decay time of residual Ca^{2+} signal, were adjusted manually to obtain close correspondence between model predictions and the phenotypes observed in the experiments presented in this manuscript. For simulations of the model lacking Doc2α, k_{2+} was set to 0. To simulate syt7KO conditions, f7 was set to 1. The effect of each model parameter on the quantified behavior of the model (number of vesicles docking between 5ms and 15ms, total asynchronously released vesicles at the end of the train, peak release rate of the first response, and the ratio between peak release rate of the first and the tenth response) was determined on a range from one-tenth of the selected parameter value to ten-fold the selected parameter value (as in supplementary table 3).

Data availability

Full data tables underlying the Fig. 5 and 6 are available in the source data. Raw images and image analysis files are available upon request.

Code availability

Custom R, Matlab and Fiji scripts for electron microscopy analysis are available at https://github.com/shigekiwatanabe/SynapsEM. More details can be found in (66). All newly-developed code for the model will be provided upon final publication.

Figure legends

Fig. 1. Doc2α, and not syt7, drives most of the asynchronous glutamate release triggered by a single action potential in cultured hippocampal neurons.
(A) Raw iGluSnFR (A184V) traces from cultured WT mouse hippocampal neurons. A single AP was applied, and images were captured every 10 ms. Peaks that appeared at the first 10 ms timepoint were defined as synchronous release events; peaks that appeared at later time points were defined as asynchronous release events. The vertical magenta line indicates the stimulus, and the vertical dashed lines indicate the imaging frames at 10, 20, 30, 40, 50, 60, and 70 ms.
(B) Three representative traces illustrate synchronous and AR peaks. The horizontal dashed line is five-times the standard deviation of the baseline noise. Individual peaks are indicated by asterisks. Traces showing single synchronous (black) and asynchronous peaks (gray), along with a trace in which both kinds of events occurred (light gray), are shown.
(C) Color coding and binning the temporal changes in iGluSnFR signals within 70 ms after a single stimulus for WT (n=15; from 4 independent litters), Doc2α^{KO} (n=17; from 5 independent litters), syt7^{KO} (n=15; from 4 independent litters), and EGTA-AM treated neurons (n=18; from 4 independent litters). The temporal color code is red (initiation of stimulus) to purple (70 ms after the stimulus); scale bar, 5 µm. Histograms of iGluSnFR ($\Delta F/F_0$) peaks were generated using 10 ms binning. Samples were color-coded as follows: WT (gray), Doc2α^{KO} (reddish), syt7^{KO} (cyan), and EGTA-AM (orange) treated neurons. The histograms include donut graph insets to display the fraction of release in each bin.
(D) Violin plot showing the % AR (>10 ms) for each condition. One-way ANOVA, followed by Dunnett's test, was used to compare mutants against WT. *** indicates $p<0.001$.

Fig. 2. Doc2α, and not syt7, drives most of the AR triggered by a single action potential at Schaffer collaterals.
(A) Schematic of the recording scheme of hippocampal slices showing stimulation of the Schaffer collateral fibers and whole-cell patch clamp recordings of CA1 pyramidal neurons.
(B) Averaged traces of evoked EPSCs recorded from WT (n=18; from 5 independent litters), Doc2α^{KO} (n=15; from 4 independent litters), syt7^{KO} (n=19; from 6 independent litters), and EGTA-AM treated neurons (n=20; from 4 independent litters).
(C) Normalized cumulative EPSC charge transfer over 400 ms.
(D) Bar graphs, from corresponding groups in panels (B-C), summarizing the amplitude, fast and slow EPSC charge, and the fast and slow EPSC t values. One-way ANOVA, followed by Dunnett's test, was used to compare mutants against WT. **, and *** indicate $p< 0.01$, and $p<0.001$.

Fig. 3. Both Doc2α and syt7 contribute to asynchronous glutamate release during train stimulation but have opposite effects on short-term plasticity in cultured hippocampal neurons.

(A) Representative iGluSnFR images from trains of 50 APs at 10 Hz (left) or 20 Hz (right). Images on the left, middle and right each show a sum of 20 frames (200 msec) before, during, and after stimulation, respectively; scale bar, 40 µm.
(B) Representative iGluSnFR responses from WT (10 Hz: n=12; from 3 independent litters; 20 Hz: n=17; from 4 independent litters), Doc2α^{KO} (n=14; from 4 independent litters; 20 Hz: n=16; from 4 independent litters), and syt7^{KO} neurons (n=15; from 3 independent litters; 20 Hz: n=12; from 3 independent litters), stimulated at 10 Hz (top) and 20 Hz (bottom).
(C) The AR fraction was defined as iGluSnFR peaks that occurred after the first 10 ms time point (i.e., from the 20 msec time point onward), divided by the total number of peaks that occurred at all time points between each stimulus. These data are plotted as a function of the stimulus number. Mean values (bold lines) ± SEM (shaded regions) are indicated.
(D) Plot of the normalized amplitude of iGluSnFR signals evoked by 50 stimuli at 10 and 20 Hz. Insets show the first three points of each trace on expanded scales.

Fig. 4. Both Doc2α and syt7 contribute to AR during train stimulation but have opposite effects on short-term plasticity at Schaffer collaterals.
(A) Representative EPSCs triggered by 20 Hz stimulus trains using WT, Doc2α^{KO}, syt7^{KO}, and EGTA-AM treated neurons. The shaded gray areas indicate the tonic charge component that likely corresponds to AR.
(B) The peak amplitude of each EPSC during the train was normalized to the first EPSC from WT (n=12; from 4 independent litters), Doc2α^{KO} (n=11; from 3 independent litters), syt7^{KO} (n=10; from 3 independent litters), and EGTA-AM treated neurons (n=11, from 3 independent litters).
(C) Bar graph showing the total tonic charge transfer (indicated by the grey areas in panel (A)), as an index of AR, from WT, Doc2□^{KO}, syt7^{KO}, and EGTA-AM treated hippocampal slices.

Fig. 5. Doc2α, but not syt7, is required for asynchronous synaptic vesicle fusion triggered by a single action potential in cultured hippocampal neurons.
(A-D) Example transmission electron micrographs of syt7^{WT} (A), syt7^{KO} (B), Doc2α^{WT} (C), and Doc2α^{KO} (D) synapses frozen at the indicated time points after an action potential (AP) or without stimulation (no stim). Arrows indicate pits in the active zone, which are presumed to be synaptic vesicles that have fused with the plasma membrane.
(E) The number of pits in the active zone per synaptic profile (part of the synapse captured in a 2D section) in syt7 wild-type littermate controls and knockouts. Error bars indicate 95% confidence interval of the mean for all data pooled together; each dot indicates the mean from a single biological replicate. Inset: same data from the 11 ms time point from each genotype, with lesser y axis range; lines indicate data are from the same biological replicate (experiment), *not* that they are paired. *P* values are from comparisons between wild-type controls (no stim, $n = 217$; 5 ms, $n = 216$; 11 ms, $n = 217$; 14 ms, $n = 230$ synaptic profiles) and knockouts (no

stim, $n = 193$; 5 ms, $n = 215$; 11 ms, $n = 230$; 14 ms, $n = 212$ synaptic profiles) frozen at the same time point.
(F) same as E, but for Doc2α wild-type controls (no stim, $n = 327$; 5 ms, $n = 229$; 11 ms, $n = 336$; 14 ms, $n = 192$ synaptic profiles) and knockouts (no stim, $n = 330$; 5 ms, $n = 231$; 11 ms, $n = 352$; 14 ms, $n = 321$ synaptic profiles).
Number of biological replicates (from separate cultures frozen on different days and analyzed in separate randomized batches): 2 for each of the syt7 time points, 2 for 5 ms and 14 ms Doc2 WT, 2 for 5 ms and 11 ms Doc2 KO, 3 for Doc2 WT no stim and 11 ms, 3 for Doc2 KO no stim and 14 ms. The numbers of pits between wild type and knockout were compared using Brown-Forsythe ANOVAs with post-hoc Games-Howell's multiple comparisons tests. In pairwise tests, the same time point for wild type vs. knockout as well as each time point within each genotype were compared against each other (only comparisons between the same time point for wild type vs. knockout are shown, see Supplementary Table 1 for all pairwise comparisons). See Source Data 1 for data used to generate the graphs shown. See Fig. S6A for active zone sizes from each condition and Fig. S6B for pit data normalized to the size of active zones.

Fig. 6. Syt7 is absolutely required for transient docking, while docked vesicles recover more quickly without Doc2α.
(A-D) Example transmission electron micrographs of syt7^{WT} (A), syt7^{KO} (B), Doc2α^{WT} (C), and Doc2α^{KO} (D) synapses frozen at the indicated time points after an action potential (AP) or without stimulation (no stim). Arrows indicate docked vesicles (synaptic vesicles with no visible distance between their membrane and the plasma membrane).
(E) The number of docked vesicles per synaptic profile (part of the synapse captured in a 2D section) in syt7 wild-type littermate controls and knockouts. Error bars indicate 95% confidence interval of the mean for all data pooled together; each dot indicates the mean from a single biological replicate. *P* values are from comparisons between wild-type controls (no stim, $n = 217$; 5 ms, $n = 216$; 11 ms, $n = 217$; 14 ms, $n = 230$ synaptic profiles) and knockouts (no stim, $n = 193$; 5 ms, $n = 215$; 11 ms, $n = 230$; 14 ms, $n = 212$ synaptic profiles) frozen at the same time point.
(F) same as E, but for Doc2α wild-type controls (no stim, $n = 327$; 5 ms, $n = 229$; 11 ms, $n = 336$; 14 ms, $n = 192$ synaptic profiles) and knockouts (no stim, $n = 330$; 5 ms, $n = 231$; 11 ms, $n = 352$; 14 ms, $n = 321$ synaptic profiles).
Number of biological replicates (from separate cultures frozen on different days and analyzed in separate randomized batches): 2 for each of the syt7 time points, 2 for 5 ms and 14 ms Doc2 WT, 2 for 5 ms and 11 ms Doc2 KO, 3 for Doc2 WT no stim and 11 ms, 3 for Doc2 KO no stim and 14 ms. The numbers of pits between wild type and knockout were compared using Brown-Forsythe ANOVAs with post-hoc Games-Howell's multiple comparisons tests. In pairwise tests, the same time point for wild type vs. knockout as well as each time point within each genotype were compared against each other (only comparisons between the same time point for wild type vs. knockout are shown, see Supplementary Table 2 for all pairwise comparisons). See Source

Data 2 for data used to generate the graphs shown. See Fig. S6A for active zone sizes from each condition, Fig. S6C for docked vesicle data normalized to the size of active zones, and Fig. S6D for distribution of undocked vesicles.

Fig. 7. A mathematical model in which syt7 catalyzes synaptic vesicle docking and Doc2α promotes fusion can qualitatively explain the observed phenotypes.
(A) Simplified scheme of the model in which syt7 acts as a catalyst of docking (increasing both docking and undocking rates) and Doc2α regulates fusion together with syt1. All proteins only exert their effect when bound to Ca^{2+}. In the model a release site can either be empty or occupied by a tethered or a docked vesicle. For full model scheme see Fig. S7.
(B) Calcium transient used to perform the simulations. The transient corresponds to a signal induced by 10 APs at 20 Hz. Insert shows a zoom-in over the first 5 ms of the transient.
(C) Average number of Ca^{2+}-ions bound to syt1, Doc2α and syt7 over time. Syt1 can maximally bind five Ca^{2+}-ions, Doc2α and syt7 can each bind two Ca^{2+}-ions. Insert shows zoom-in over the first 5 ms of the simulation.
(D) The number of docked vesicles over time for simulations including functionality of all proteins (black, WT), simulations lacking Doc2α (magenta, Doc2α-) and simulations lacking syt7 (cyan, syt7-). Insert shows a zoom-in over the first 15ms of the simulation. (E) Simulated release rates obtained using the full model (WT, left, black), the model lacking Doc2α (Doc2α -, middle, magenta) and the model lacking syt7 (syt7, right, cyan) simulations. Top line shows the entire trace. Bottom panels show a zoom-in to illustrate the asynchronous release component, which is indicated by the gray area.
(F) Cumulative number of asynchronously released vesicles per stimulus. Asynchronous release is quantified as the release between 5ms after the start of the AP and the start of the next AP. Insert shows zoom-in over the first two pulses.
(G) Peak release rates per stimulus for stimulations using the full model (WT, black), the model lacking Doc2α (Doc2α-, magenta) and the model lacking syt7 (syt7-, cyan).

Fig. 8. AR in Doc2α/syt7 DKO neurons: non-additive effects on AR indicate function through a common pathway.
All recordings were carried out using acute hippocampal slices, in CA1, as described in Fig. 2 and 4.
(A) Averaged traces of evoked EPSCs recorded from WT (n=18; from 5 independent litters), Doc2αKO (n=15; from 4 independent litters), Doc2α/syt7 DKO (n=14; from 4 independent litters), and EGTA-AM treated neurons (n=20; from 4 independent litters).
(B) Bar graph summarizing the slow EPSC charge values. One-way ANOVA, followed by Dunnett's test, was used to compare mutants against WT. **, and *** indicate $p< 0.01$, and $p<0.001$.

(C) Representative EPSCs triggered by 20 Hz stimulus trains using WT and Doc2α/syt7 DKO (n=15; from 5 independent litters) neurons.
(D) AR in WT, Doc2αKO, syt7KO, Doc2α/syt7 DKO, and EGTA-AM treated neurons was estimated by measuring the total tonic charge transfer during the 20 Hz stimulus train, as described in Fig. 4C.

Fig. S1. Expression of iGluSnFR in cultured hippocampal neurons.
(A) Representative serial frames of iGluSnFR fluorescence from the WT, Doc2α^{KO}, and syt7^{KO} neurons, before and after eliciting a single action potential (AP; arrow); the heatmap is shown on the right.
(B) The relaxation rate of iGluSnFR (A184V). Averaged iGluSnFR signals from 254 boutons from WT hippocampal neurons after a single stimulus (filled circles). Data were fitted with a single exponential function (solid line), and the decay τ value is indicated.
(C) iGluSnFR peak amplitudes ($\Delta F/F_0$ at 10 ms), a single action potential, from WT, Doc2a KO, and syt7 KO neurons.

Fig. S2. Additional raw iGluSnFR traces during 20 Hz train stimulation, and paired-pulse ratios from the first two responses at 10 and 20 Hz.
(A) Raw 20 Hz iGluSnFR traces from cultured WT, Doc2α^{KO}, and syt7^{KO} hippocampal neurons. In the lower panel, responses from the last five stimuli are overlayed, revealing a qualitative reduction in AR peaks in Doc2α and syt7 KO neurons.
(B) Mean paired-pulse ratios (peak iGluSnFR signal from the 2nd stimulus divided by peak signal from the 1st stimulus during the 10Hz and 20 Hz train stimulation) at different interstimulus intervals (Δt) recorded in cultured hippocampal neurons isolated from WT, Doc2α^{KO}, and syt7^{KO} mice. Data points here are mean values ± SEM. One-way ANOVA, followed by Dunnett's test, was used to compare mutants against WT. *** indicates $p<0.001$.

Fig. S3. Spatial distribution of AR, measured via iGluSnFR imaging, in cultured hippocampal neurons.
(A) Schematic illustrating AR distribution patterns at axon terminals; the large shaded grey circles depict the soma; small circles depict presynaptic boutons. For this analysis, only AR was analyzed, using data collected from 923 ROIs that were initially identified because they yielded at least one evoked response (AR, synchronous, or both) in the first three stimuli from a 10 Hz train. Boutons that exhibit AR, for the indicated position and stimulus, are orange; open circles indicate boutons that did not exhibit AR at the indicated position or stimulus. All of the AR distribution patterns in each of the four sub-panels are from the same boutons at the same fixed positions. For convenience, only twelve boutons are shown, and these are numbered 1-12 to emphasize that the same boutons are analyzed in each of the sub-panels. The organization of these boutons was artificially grouped to some extent, to better visualize the patterns of release between each stimulus. The bottom left table quantifies the ratio of AR patterns: AR to AR, AR

to no AR, no AR to AR, and no AR to no AR, from the first to the second stimulus. The same analysis, but between the second and third stimulus, is provided in the bottom right table. The distribution of AR to target cells in the first versus the second pulses is similar to the distribution between the third and fourth pulses. These data suggest that AR during the first pulse, while molecularly distinct, does not segregate to different target cells, as compared to AR elicited by subsequent stimuli.
(B) Table summarizing the fraction of boutons with the same responses after the initial three stimuli. AR only; represents pure AR that successively occurred three times at the same bouton, in the absence of SR. Synchronous release (SR) only; indicates boutons that exhibited purely SR during the first three stimuli, in the absence of AR. AR; reflects AR that occurred at the same bouton for all three successive stimuli regardless of the presence or absence of SR.
Interpretation: In the main text we noted that spatial segregation of AR during the first two responses was not observed. Expanding on this further, the same pattern was observed when comparing the second and third responses. Moreover, nearly 70% of all responding boutons exhibited AR at least once during the first three stimuli in a train, either with or without a concurrent synchronous component (panel 2A). So, even though AR presents only a third of the charge transfer in our experiments (Fig. 1C,E, and 2D), this mode of release is widespread. In addition, 40% of all responding boutons analyzed exhibited AR in all three of the initial stimuli in a train, and approximately half of the boutons that had AR after the first stimulus also yielded AR during the second stimulus (panel 2B). In contrast, only 6% and 8% of boutons exhibited pure AR or synchronous responses, respectively, in response to all three initial stimuli in a train (panel 2B). While our data argue against the segregation of AR during the first response, it remains possible that further analysis, of much larger data sets, using sensitive algorithms, could reveal more subtle differences that might have escaped detection.

Fig. S4. AR in acute brain slices from Doc2α and syt7 KO mice during 10 Hz train stimulation.
(A) Representative hippocampal slice from a WT mouse.
(B) A stimulating electrode was placed in the Schaffer collateral pathway and transmission to CA1 neurons was monitored via whole-cell patch clamp recordings.

Fig. S5. Additional example transmission electron micrographs.
From the experiments described in Fig. 5 and Fig. 6. Scale bar: 100 nm.

Fig. S6. Additional quantification from electron microscopy.
From the experiments described in Fig. 5 and Fig. 6.
(A) Size of the active zone in each synaptic profile from each condition. Each dot indicates a single synaptic profile. Error bars: median and interquartile range.
(B) Same pit data from Fig. 5, normalized to the size of the active zone in each condition. “Per 500 nm of active zone” calculation was performed by multiplying the count from each synaptic

profile by 500 and dividing by the mean active zone size from the data set (i.e., normalization was not performed by the size of the active zone in each individual synaptic profile).
(C) Same as B, but for docked vesicle data from Fig. 6.
(D) Distances of undocked synaptic vesicles from the plasma membrane at the active zone, not including docked vesicles (which are 0 nm from the plasma membrane). Distances are binned in 5-nm increments ("5" indicates vesicles 0.1–5 nm from the membrane, "10" indicates 6–10 nm, and so on). Each dot indicates the mean number of synaptic vesicles per synaptic profile in that distance range from the active zones. See Source Data 3 for data used to generate the graphs.

Fig. S7. Full reaction scheme of the model
In the model a release site can be in three different states: empty, occupied with a tethered vesicle or a docked vesicle. Within those states a release site can be in a different substate depending on the number of Ca^{2+} ions bound to Doc2α, syt7 and syt1. The top left illustration shows the legend for these substates. Doc2α and syt7 are assumed to be part of the release sites. Therefore, syt7 and Doc2α can bind to Ca^{2+} in all the states. Syt1 can only bind to Ca^{2+} once the vesicle is docked. Binding of Ca^{2+} to syt7 increases both the docking and undocking rates (as indicated by the color coding and the length of the *docking* and *undocking* arrows). Ca^{2+} binding to Doc2α and syt1 increases the fusion probability of the docked vesicles (green to red color coding for low to high fusion rates, respectively. For full description of the model see methods.

Fig. S8. Effect of different model parameters on model predictions.
(A) Effect of varying model parameters on the number of vesicles docking between 15 and 5ms.
(B) Effect of varying model parameters on total number of asynchronously released vesicles.
(C) The effect of varying model parameters on the peak release rate at the first pulse.
(D) The effect of varying model parameters on the ratio between the peak release rates of the tenth and the first pulse.
Each parameter was evaluated at 19 values ranging from one-tenth of the selected value (as presented in supplementary table 3) to ten-fold the selected parameter value. Model parameters were varied for WT (black), Doc2α- (magenta) and syt7- (cyan) simulations. For Ca^{2+}-binding rates (k_{2+} and k_{7+}), the unbinding rates were adjusted accordingly to have a constant Ca^{2+}-affinity. Similarly, the untethering and undocking rates were adjusted with the tethering and docking.

Fig. S9. Covarying two parameters illustrates that the selected model parameters are unlikely to provide a unique solution.
(A) Effect of covarying two model parameters on the number of vesicles docking between 15 and 5ms.
(B) Effect of covarying two model parameters on total number of asynchronously released vesicles.
(C) The effect of covarying two model parameters on the peak release rate at the first pulse.

(D) The effect of covarying two model parameters on the ratio between the peak release rates of the tenth and the first pulse.
Each parameter was evaluated at 19 values ranging from one-tenth of the selected value (as presented in supplementary table 3) to ten-fold the selected parameter value. The selected setting (represented in Fig. 7) is the middle point in each panel. Covarying the Ca^{2+}-binding rate of syt7 (k_{7+}) with the effect syt7 has on the docking and undocking rates (f_7, top panels) shows that there is a section in the parameter space where WT simulations result in similar quantified model predictions (as indicated by the same colors in the heatmaps). This also holds for covarying the Ca^{2+}-binding rate of Doc2α (k_{2+}) with the decay time of the residual Ca^{2+}-signal (tau, middle panels) and covarying of f_2 with the amplitude of the residual Ca^{2+}-signal (bottom, panels). Together this illustrates that the selected model parameters are unlikely to present a unique solution. For Ca^{2+}-binding rates (k_{2+} and k_{7+}), the unbinding rates were adjusted accordingly to keep a constant Ca^{2+}-affinity.

Fig. S10. Evaluation of a model lacking both Doc2α and syt7.
(A)The number of docked vesicles over time for simulations including functionality of all proteins (black, WT), simulations lacking Doc2α (magenta, Doc2α-), simulations lacking syt7 (cyan, syt7-) and simulations lacking both syt7 and Doc2α (blue, Syt7-& Doc2α-). Insert shows a zoom-in over the first 15 ms of the simulation.
(B) Simulated release rates obtained using a model lacking syt7 and Doc2α (Syt7-& Doc2α-, blue). Top panel shows the entire trace. Bottom panel show a zoom-in to illustrate the asynchronous release component, which is indicated by the gray area.
(C) Cumulative number of asynchronously released vesicles per stimulus. Asynchronous release is quantified as the release between 5 ms after the start of the AP and the start of the next AP. Insert shows zoom-in over the first 2 pulses.
(D) Peak release rates per stimulus for stimulations using the full model (black, WT), simulations lacking Doc2α (magenta, Doc2α-), simulations lacking syt7 (cyan, syt7-) and simulations lacking both syt7 and Doc2α (blue, Syt7-& Doc2α-).

Fig. S11. Synaptic depression of phasic responses in Doc2α/syt7 DKOs, compared to single KO and AM-EGTA treated conditions.
Recordings of CA1 neurons in hippocampal slices were carried out as described in Fig. 4. The peak amplitude of each EPSC during 50 APs at 20Hz was normalized to the first EPSC from Doc2α/syt7 DKO slices; for comparison, all other conditions were replotted from Fig. 4. As predicted, the depression phenotype of the DKO lies between the Doc2α and syt7 depression curves but mimics the syt7 KO by the end of the train.

Fig. S12. Doc2α-triggers AR in response to single action potentials; during repetitive stimulation, syt7 mediates transient docking to feed docked vesicles to Doc2α for ongoing AR.

At rest, synaptic vesicles are docked at the active zone (solid gray line) in a dynamic equilibrium indicated by the antiparallel black arrows (far left panel). Under these conditions, docking is not affected by syt7 (Fig. 6E; Vevea et al. (2021). A single action potential triggers both undocking (UD) and synchronous release (SR), resulting in a 40% reduction in docked vesicles in ~5 ms (Fig. 6E,F; Kusick et al., 2020). This is followed by a transient docking (TD) step in which vesicles re-attach to the active zone via a process that takes 14 msec and is mediated by Ca^{2+} and syt7 (granite green) (Fig. 6E,F; Kusick et al., 2020;). The same single AP also triggers AR mediated directly by Doc2α (lilac), at the 11 ms time point (Fig. 5F; Yao et al., 2011). Syt7 plays no role in release during the first action potential (Fig. 1,2, and 5E; and references in the main text), again because it does not regulate docking in the resting state. However, loss of syt7 abolishes activity-dependent TD (Fig. 6E), which decreases the availability of docked vesicles during subsequent (i.e., two or more) action potentials, indirectly reducing Doc2α-triggered AR during ongoing activity. As a test of this model, an epistasis experiment revealed that the Doc2α/syt7 DKO AR phenotype was non-additive (Fig. 8). This validates a sequential, two-step, model, in which—during ongoing activity—syt7 feeds docked vesicles to Doc2α, which directly mediates AR. Hence, syt7 acts upstream of Doc2α, as a docking factor, while Doc2α functions as the proximal Ca^{2+} sensor for AR in hippocampal synapses. This model can account for why only Doc2α drives AR in response to a single action potential, while Doc2α and syt7 contribute equally to AR during subsequent action potentials.

Supplementary table 3

Parameter name	Description	Value
N_{sites}	Number of available release sites (limits the number of docked/tethered vesicles)	200
k_{tet}	Tethering rate	7 s^{-1}
k_{untet}	Untethering rate constant	7 s^{-1} (same as k_{tet})
$k_{docking}$	Docking rate constant	5 s^{-1}
$k_{undocking}$	Undocking rate constant	5 s^{-1} (same as $k_{docking}$)
l_{+}	Syt1 and Doc2 independent fusion rate constant / basal fusion rate	3.5e-4 s^{-1} (57)
Parameters Ca^{2+}-transient		

Amplitude	Amplitude of synchronous Ca^{2+} transient in response to AP	30 µM
Residual Ca^{2+} amplitude	Amplitude of the residual Ca^{2+} signal (following single-exponential decay)	0.75 µM
Tau	Decay time constant of residual Ca^{2+} signal	0.2s
Ca^{2+}_{rest}	Resting calcium concentration	0.05 µM
Parameters syt7		
N_7	Ca^{2+} cooperativity of syt7	2
K_{D7}	Dissociation constant, syt7	1.5 µM (67)
k_{7+}	Ca^{2+} binding rate, syt7	28 $\mu M^{-1} s^{-1}$
k_{7-}	Ca^{2+} unbinding rate constant, syt7	42 s^{-1}
b_7	Cooperativity factor, syt7	0.5
f_7	Effect single Ca^{2+} binding to syt7 has on $k_{docking}$ and $k_{undocking}$	10 (1 for syt7- simulations)
Parameters doc2α		
N_2	Ca^{2+} cooperativity of Doc2α	2 (same as for syt7)
K_{D2}	Dissociation constant, Doc2α	1.5 µM (same as for syt7)
k_{2+}	Ca^{2+} binding rate, Doc2α	28 $\mu M^{-1} s^{-1}$ (5x reduction compared to syt1, based on (8); 0 for Doc2α- simulations.
k_{2-}	Ca^{2+} unbinding rate constant, Doc2α	42 s^{-1} (Computed using K_{D2})
b_2	Cooperativity factor, Doc2α	0.5 (same as for syt7)
f_2	Effect single Ca^{2+} binding to Doc2α has on the fusion rate	16

Parameters syt1		
N_1	Ca^{2+} cooperativity of Syt1	5 (57)
k_{1+}	Ca^{2+} binding rate, Syt1	140 μM^{-1} s^{-} (57)
k_{1-}	Ca^{2+} unbinding rate constant, syt1	4000 s^{-1} (57)
b_1	Cooperativity factor, syt1	0.5 (57)
f_1	Effect single Ca^{2+} binding to Syt1 has on the fusion rate	27.98 (57)

References

1. B. L. Sabatini, W. G. Regehr, Timing of neurotransmission at fast synapses in the mammalian brain. *Nature* **384**, 170–172 (1996).
2. P. S. Kaeser, W. G. Regehr, Molecular mechanisms for synchronous, asynchronous, and spontaneous neurotransmitter release. *Annu. Rev. Physiol.* **76**, 333–63 (2014).
3. Y. Goda, C. F. Stevens, Two components of transmitter release at a central synapse. *Proc. Natl. Acad. Sci.* **91**, 12942–12946 (1994).
4. C. F. Stevens, J. M. Sullivan, The synaptotagmin C2A domain is part of the calcium sensor controlling fast synaptic transmission. *Neuron* **39**, 299–308 (2003).
5. K. J. Iremonger, J. S. Bains, Integration of Asynchronously Released Quanta Prolongs the Postsynaptic Spike Window. *J. Neurosci.* **27**, 6684–6691 (2007).
6. F. Manseau, *et al.*, Desynchronization of neocortical networks by asynchronous release of GABA at autaptic and synaptic contacts from fast-spiking interneurons. *PLoS Biol.* **8** (2010).
7. M. Jiang, *et al.*, Enhancement of asynchronous release from fast-spiking interneuron in human and rat epileptic neocortex. *PLoS Biol.* **10** (2012).
8. J. Yao, J. D. Gaffaney, S. E. Kwon, E. R. Chapman, Doc2 is a Ca 2+ sensor required for asynchronous neurotransmitter release. *Cell* **147**, 666–677 (2011).
9. R. Xue, J. D. Gaffaney, E. R. Chapman, Structural elements that underlie Doc2β function during asynchronous synaptic transmission. *Proc. Natl. Acad. Sci.* **112**, E4316–E4325 (2015).
10. E. Hui, *et al.*, Three distinct kinetic groupings of the synaptotagmin family: candidate sensors for rapid and delayed exocytosis. *Proc. Natl. Acad. Sci. U. S. A.* **102**, 5210–4 (2005).
11. J. D. Gaffaney, R. Xue, E. R. Chapman, P. J. Brennwald, Mutations that disrupt Ca 2 + -binding activity endow Doc2 β with novel functional properties during synaptic transmission. *Mol. Biol. Cell* **25**, 481–494 (2014).
12. R. Xue, *et al.*, Doc2-mediated superpriming supports synaptic augmentation. *Proc. Natl. Acad. Sci. U. S. A.* **115**, E5605–E5613 (2018).
13. M. M. Khan, W. G. Regehr, Loss of doc2b does not influence transmission at purkinje cell to deep nuclei synapses under physiological conditions. *Elife* **9** (2020).
14. A. J. Groffen, *et al.*, Doc2b Is a High-Affinity Ca2+ Sensor for Spontaneous Neurotransmitter Release. *Science.* **327**, 1614–1618 (2010).
15. V. Huson, W. G. Regehr, Diverse roles of Synaptotagmin-7 in regulating vesicle fusion. *Curr. Opin. Neurobiol.* **63**, 42–52 (2020).
16. H. Wen, *et al.*, Distinct roles for two synaptotagmin isoforms in synchronous and asynchronous transmitter release at zebra fish neuromuscular junction. *Proc. Natl. Acad. Sci.* **107**, 13906–13911 (2010).
17. A. Maximov, *et al.*, Genetic analysis of synaptotagmin-7 function in synaptic vesicle exocytosis. *Proc Natl Acad Sci U S A* **105**, 3986–3991 (2008).
18. T. Bacaj, *et al.*, Synaptotagmin-1 and Synaptotagmin-7 Trigger Synchronous and Asynchronous Phases of Neurotransmitter Release. *Neuron* **80**, 947–959 (2013).
19. C. Chen, *et al.*, Triple Function of Synaptotagmin 7 Ensures Efficiency of High-Frequency Transmission at Central GABAergic Synapses. *Cell Rep.* **21**, 2082–2089 (2017).
20. J. Turecek, X. W. G. Regehr, Synaptotagmin 7 Mediates Both Facilitation and

Asynchronous Release at Granule Cell Synapses. *J. Neurosci.* **38**, 3240–3251 (2018).
21. S. Deng, *et al.*, Regulation of Recurrent Inhibition by Asynchronous Glutamate Release in Neocortex. *Neuron* **105**, 522-533.e4 (2020).
22. J. Turecek, W. G. Regehr, Neuronal Regulation of Fast Synaptotagmin Isoforms Controls the Relative Contributions of Synchronous and Asynchronous Release. *Neuron* **101** (2019).
23. G. F. Kusick, *et al.*, Synaptic vesicles transiently dock to refill release sites. *Nat. Neurosci.* **23**, 1329–1338 (2020).
24. J. S. Marvin, *et al.*, An optimized fluorescent probe for visualizing glutamate neurotransmission. *Nat. Methods* **10**, 162–170 (2013).
25. J. S. Marvin, *et al.*, Stability, affinity and chromatic variants of the glutamate sensor iGluSnFR. *Nat. Methods* **15** (2018).
26. J. D. Vevea, *et al.*, Synaptotagmin 7 is enriched at the plasma membrane through γ-secretase processing to promote vesicle docking and control synaptic plasticity in mouse hippocampal neurons. *Elife* (2021).
27. G. Sakaguchi, *et al.*, Doc2α is an activity-dependent modulator of excitatory synaptic transmission. *Eur. J. Neurosci.* **11**, 4262–4268 (1999).
28. S. Chakrabarti, *et al.*, Impaired membrane resealing and autoimmune myositis in synaptotagmin VII-deficient mice. *J. Cell Biol.* **162**, 543–549 (2003).
29. J. D. Vevea, E. R. Chapman, Acute disruption of the synaptic vesicle membrane protein synaptotagmin 1 using knockoff in mouse hippocampal neurons. *Elife* **9** (2020).
30. C. Chen, W. G. Regehr, Contributions of residual calcium to fast synaptic transmission. *J. Neurosci.* **19**, 6257–66 (1999).
31. Y. Otsu, *et al.*, Competition between Phasic and Asynchronous Release for Recovered Synaptic Vesicles at Developing Hippocampal Autaptic Synapses. *J. Neurosci.* **24**, 420–433 (2004).
32. H. Liu, *et al.*, Synaptotagmin 7 functions as a Ca2+-sensor for synaptic vesicle replenishment. *Elife* (2014) https:/doi.org/10.7554/eLife.01524.
33. S. L. Jackman, J. Turecek, J. E. Belinsky, W. G. Regehr, The calcium sensor synaptotagmin 7 is required for synaptic facilitation. *Nature* **529**, 88–91 (2016).
34. T. Miki, *et al.*, Actin- and Myosin-Dependent Vesicle Loading of Presynaptic Docking Sites Prior to Exocytosis. *Neuron* **91**, 808–823 (2016).
35. T. Miki, Y. Nakamura, G. Malagon, E. Neher, A. Marty, Two-component latency distributions indicate two-step vesicular release at simple glutamatergic synapses. *Nat. Commun.* (2018) https:/doi.org/10.1038/s41467-018-06336-5.
36. E. Neher, N. Brose, Dynamically Primed Synaptic Vesicle States: Key to Understand Synaptic Short-Term Plasticity. *Neuron* **100**, 1283–1291 (2018).
37. M. Silva, V. Tran, A. Marty, Calcium-dependent docking of synaptic vesicles. *Trends Neurosci.* **44**, 579–592 (2021).
38. G. F. Kusick, T. H. Ogunmowo, S. Watanabe, Transient docking of synaptic vesicles: Implications and mechanisms. *Curr. Opin. Neurobiol.* **74** (2022).
39. S. Chang, T. Trimbuch, C. Rosenmund, Synaptotagmin-1 drives synchronous Ca2+-triggered fusion by C2B-domain-mediated synaptic-vesicle-membrane attachment. *Nat. Neurosci.* **21**, 33–42 (2018).
40. J. R. L. Kobbersmed, *et al.*, Rapid regulation of vesicle priming explains synaptic facilitation despite heterogeneous vesicle:Ca 2+ channel distances. *Elife* (2020).

41. K. Blanchard, *et al.*, Differentially poised vesicles underlie fast and slow components of release at single synapses. *J. Gen. Physiol.* **152** (2020).
42. S. Li, *et al.*, Asynchronous release sites align with NMDA receptors in mouse hippocampal synapses. *Nat. Commun.* **12**, 1–13 (2021).
43. A. M. Walter, P. S. Pinheiro, M. Verhage, J. B. Sørensen, A Sequential Vesicle Pool Model with a Single Release Sensor and a Ca 2 + -Dependent Priming Catalyst Effectively Explains Ca 2 + -Dependent Properties of Neurosecretion. *PLoS Comput. Biol.* **9** (2013).
44. S. Sugita, *et al.*, Synaptotagmin VII as a Plasma Membrane Ca 2+ Sensor in Exocytosis. *Neuron* **30**, 459–473 (2001).
45. J. P. Weber, T. L. Toft-Bertelsen, R. Mohrmann, I. Delgado-Martinez, J. B. Sørensen, Synaptotagmin-7 is an asynchronous calcium sensor for synaptic transmission in neurons expressing SNAP-23. *PLoS One* **9** (2014).
46. M. Verhage, *et al.*, DOC2 proteins in rat brain: Complementary distribution and proposed function as vesicular adapter proteins in early stages of secretion. *Neuron* **18**, 453–461 (1997).
47. A. Radhakrishnan, A. Stein, R. Jahn, D. Fasshauer, The Ca2+ affinity of synaptotagmin 1 is markedly increased by a specific interaction of its C2B domain with phosphatidylinositol 4,5-bisphosphate. *J. Biol. Chem.* **284**, 25749–25760 (2009).
48. J. Bai, W. C. Tucker, E. R. Chapman, PIP2 increases the speed of response of synaptotagmin and steers its membrane-penetration activity toward the plasma membrane. *Nat. Struct. Mol. Biol.* **11**, 36–44 (2004).
49. J. Sun, *et al.*, A dual-Ca2+-sensor model for neurotransmitter release in a central synapse. *Nature* **450**, 676–682 (2007).
50. S. L. Jackman, W. G. Regehr, The Mechanisms and Functions of Synaptic Facilitation. *Neuron* **94**, 447–464 (2017).
51. P. R. F. Mendonça, *et al.*, Asynchronous glutamate release is enhanced in low release efficacy synapses and dispersed across the active zone. *Nat. Commun.* (2022) https:/doi.org/10.1038/s41467-022-31070-4.
52. A. Honigmann, *et al.*, Phosphatidylinositol 4,5-bisphosphate clusters act as molecular beacons for vesicle recruitment. *Nat. Struct. Mol. Biol.* **20** (2013).
53. Q. Zhou, *et al.*, Architecture of the Synaptotagmin-SNARE Machinery for Neuronal Exocytosis. *Nature* **525**, 62–67 (2015).
54. Q. Zhou, *et al.*, The primed SNARE-complexin-synaptotagmin complex for neuronal exocytosis. *Nature* **548**, 420–425 (2017).
55. Y. Chen, *et al.*, Synaptotagmin-1 interacts with PI(4,5)P2 to initiate synaptic vesicle docking in hippocampal neurons. *Cell Rep.* **34**, 108842 (2021).
56. J. R. L. Kobbersmed, M. M. M. Berns, S. Ditlevsen, J. B. Sørensen, A. M. Walter, Allosteric stabilization of calcium and phosphoinositide dual binding engages three synaptotagmins in fast exocytosis. *bioRxiv* (2022) https:/doi.org/https://doi.org/10.1101/2021.10.22.465434.
57. O. Kochubey, R. Schneggenburger, Synaptotagmin Increases the Dynamic Range of Synapses by Driving Ca 2 + -Evoked Release and by Clamping a Near-Linear Remaining Ca 2 + Sensor. *Neuron* **69**, 736–748 (2011).
58. M. Schupp, *et al.*, Interactions Between SNAP-25 and Synaptotagmin-1 Are Involved in Vesicle Priming, Clamping Spontaneous and Stimulating Evoked Neurotransmission. *J.*

Neurosci. **36**, 11865–11880 (2016).
59. N. A. Courtney, H. Bao, J. S. Briguglio, E. R. Chapman, Synaptotagmin 1 clamps synaptic vesicle fusion in mammalian neurons independent of complexin. *Nat. Commun.* (2019) https:/doi.org/10.1038/s41467-019-12015-w.
60. T. -i. Nishiki, Synaptotagmin I Synchronizes Transmitter Release in Mouse Hippocampal Neurons. *J. Neurosci.* **24**, 6127–6132 (2004).
61. A. Maximov, T. C. Südhof, Autonomous Function of Synaptotagmin 1 in Triggering Synchronous Release Independent of Asynchronous Release. *Neuron* **48**, 547–554 (2005).
62. K. Lin, H. Taschenberger, E. Neher, A sequential two-step priming scheme reproduces diversity in synaptic strength and short-term plasticity. *Proc. Natl. Acad. Sci. U. S. A.* **119**, e2207987119 (2022).
63. I. H. Cho, *et al.*, The potassium channel subunit Kvβ1 serves as a major control point for synaptic facilitation. *Proc. Natl. Acad. Sci. U. S. A.* **117**, 29937–29947 (2020).
64. M. Bendahmane, *et al.*, Synaptotagmin-7 enhances calcium-sensing of chromaffin cell granules and slows discharge of granule cargos. *J. Neurochem.* **154**, 598–617 (2020).
65. G. E. Truett, *et al.*, Preparation of PCR-quality mouse genomic dna with hot sodium hydroxide and tris (HotSHOT). *Biotechniques* **29**, 52–54 (2000).
66. S. Watanabe, M. W. Davis, G. F. Kusick, J. Iwasa, E. M. Jorgensen, SynapsEM: computer-assisted synapse morphometry. *Front. Synaptic Neurosci.* (2020) https:/doi.org/10.3389/FNSYN.2020.584549.
67. D. S. Brandt, M. D. Coffman, J. J. Falke, J. D. Knight, Hydrophobic contributions to the membrane docking of synaptotagmin 7 C2A domain: Mechanistic contrast between isoforms 1 and 7. *Biochemistry* **51**, 7654–7664 (2012).

Acknowledgments
We thank J.D. Vevea, M.M. Bradberry, K.C. Courtney, D. Larson, C. Greer, R.A. Pearce, and M. Seibert for help with iGluSnFR imaging, maintaining mouse strains, and data analysis and interpretation. We thank M. Seibert for developing the polymerase chain reaction protocol for Doc2α genotyping. We thank S. Myers for recommending the alkaline lysis DNA prep protocol for genotyping. We thank all other members of the Chapman and Watanabe labs for helpful feedback and discussions. This work was funded by the National Institutes of Health (MH061876 and NS097362 to E.R.C.;1DP2 NS111133-01 and 1R01 NS105810-01A1 to S.W.), the National Science Foundation (1727260 to S.W.). E.R.C. is an Investigator of the Howard Hughes Medical Institute. S.W. is an Alfred P. Sloan fellow, a McKnight Foundation Scholar and a Klingenstein and Simons Foundation scholar. A.M.W. was supported by a Young Investigator Award from the Novo Nordisk Foundation (NNF19OC0056047). G.F.K. was supported by a grant from the National Institutes of Health to the Biochemistry, Cellular and Molecular Biology program of the Johns Hopkins University School of Medicine (T32 GM007445), a National Science Foundation Graduate Research Fellowship (2016217537), and is a Hay Fellow of the Johns Hopkins University School of Medicine Department of Cell Biology. The EM ICE high-pressure freezer was purchased partly with funds from an equipment grant from the National Institutes of Health (S10RR026445) awarded to S. C. Kuo. This article is subject to HHMI's Open Access to Publications policy. HHMI lab heads have previously granted a nonexclusive CC BY 4.0 license to the public and a sublicensable license to HHMI in their research articles. Pursuant to those licenses, the author-accepted manuscript of this article can be made freely available under a CC BY 4.0 license immediately upon publication.

Author contributions

Z.W., G.F.K., E.R.C., M.M.M.B., A.M.W., and S.W. designed the study and wrote the manuscript. Z.W. performed all iGluSnFR and electrophysiology experiments, analyzed the corresponding data, and generated the corresponding figures. G.F.K. performed all electron microscopy experiments, with help from S.R, analyzed the corresponding data with S.W., and generated the corresponding figures with S.W. M.M.M.B. and A.M.W. performed simulations. K.I., S.R., and G.F.K. performed knockout cell culture for the electron microscopy experiments. E.R.C. and S.W. funded and oversaw the research.

Ethics declarations

Competing interests

The authors declare no competing interests.

Figure 1

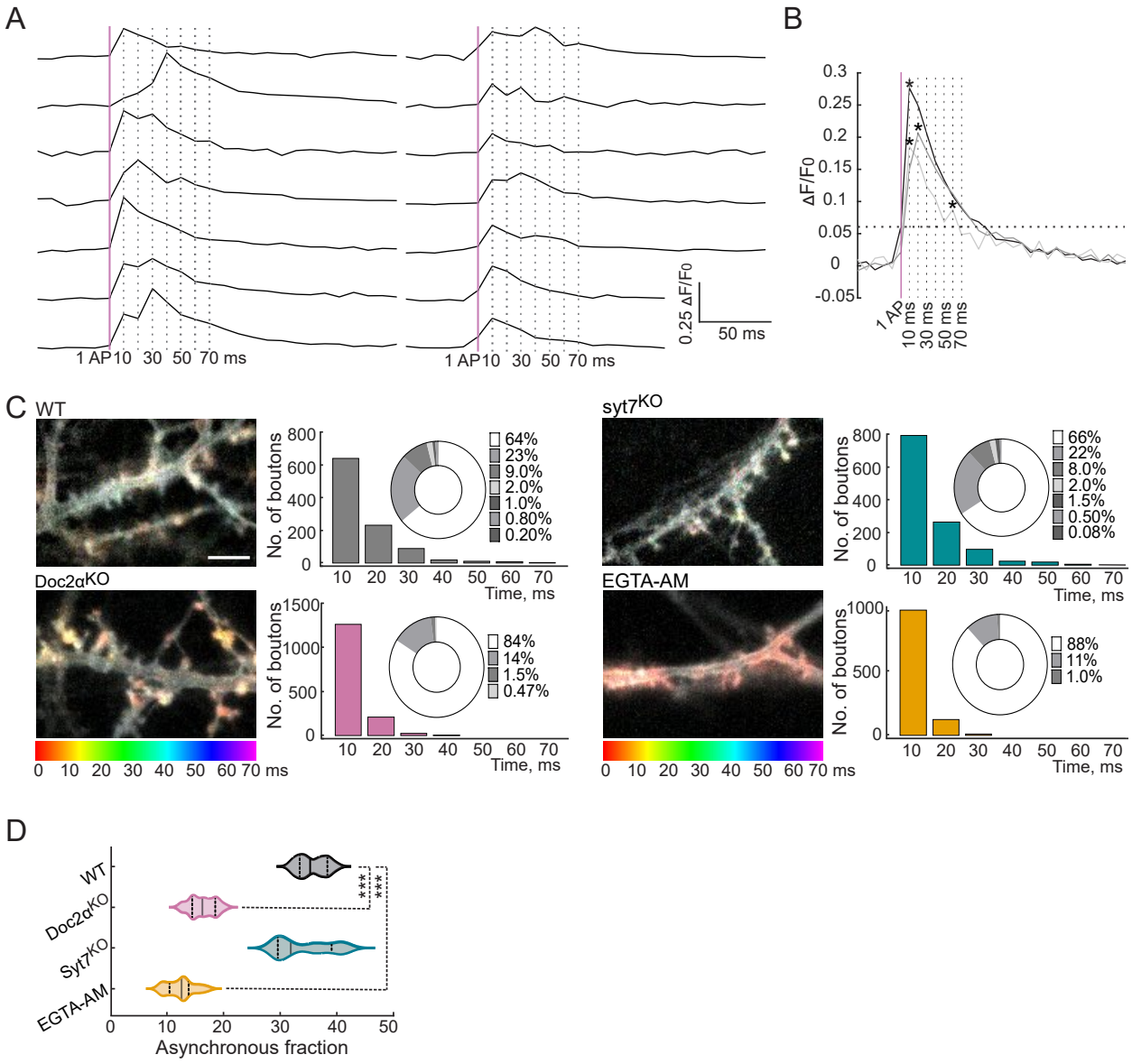
A
1 AP 10 30 50 70 ms
1 AP 10 30 50 70 ms
0.25 ΔF/F0
50 ms
B
ΔF/F0
1 AP
10 ms
30 ms
50 ms
70 ms
C
WT
No. of boutons
Time, ms
64%
23%
9.0%
2.0%
1.0%
0.80%
0.20%
syt7KO
66%
22%
8.0%
2.0%
1.5%
0.50%
0.08%
Doc2αKO
84%
14%
1.5%
0.47%
EGTA-AM
88%
11%
1.0%
0 10 20 30 40 50 60 70 ms
D
WT
Doc2αKO
Syt7KO
EGTA-AM
Asynchronous fraction

Figure 2

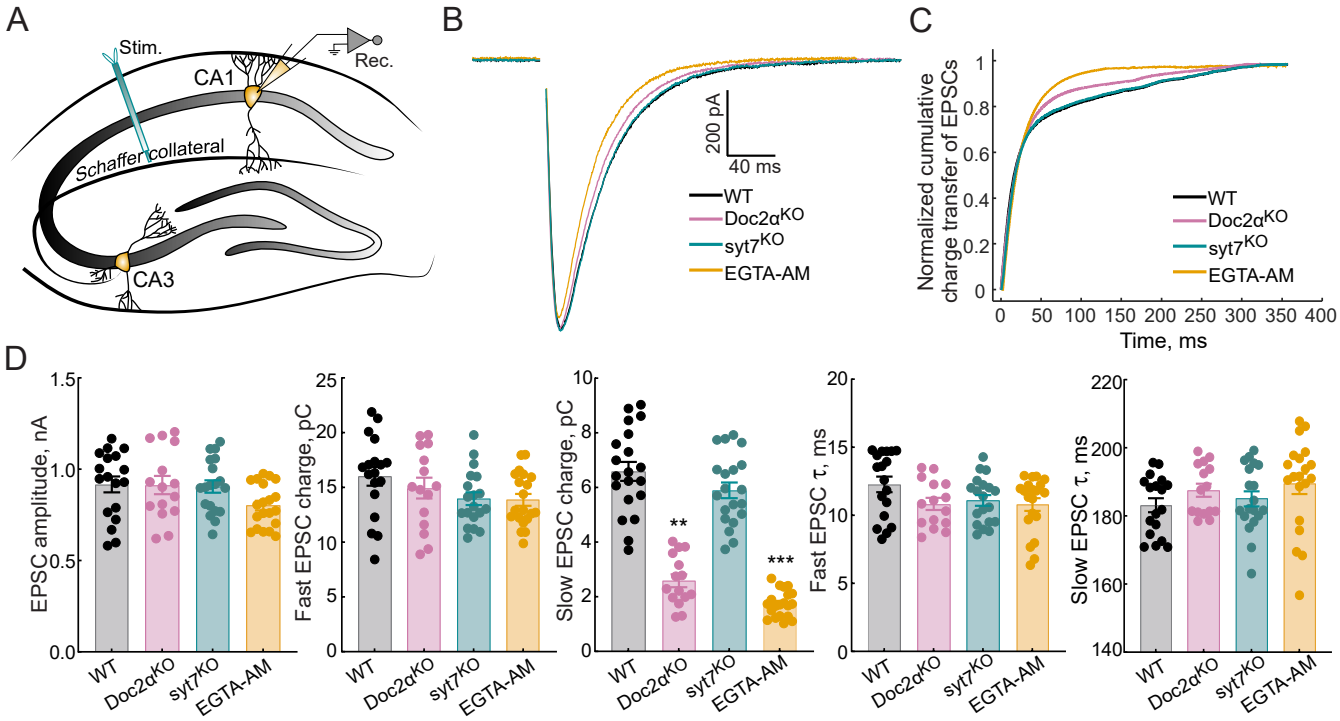
A
Stim.
Rec.
CA1
Schaffer collateral
CA3
B
200 pA
40 ms
WT
Doc2α^KO
syt7^KO
EGTA-AM
C
Normalized cumulative charge transfer of EPSCs
Time, ms
D
EPSC amplitude, nA
Fast EPSC charge, pC
Slow EPSC charge, pC
Fast EPSC τ, ms
Slow EPSC τ, ms
**
***
WT
Doc2αKO
syt7KO
EGTA-AM

Figure 3

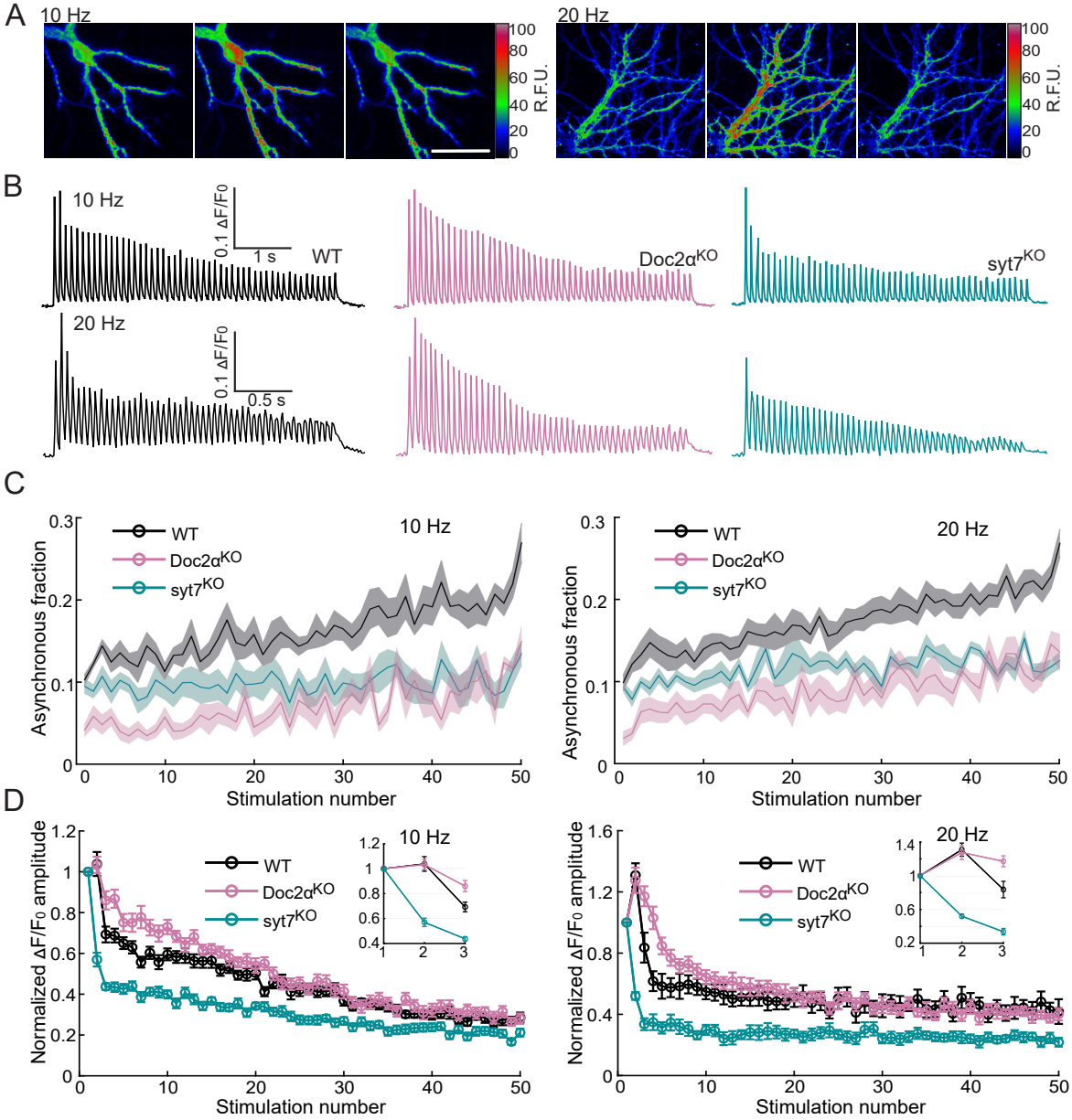
A
10 Hz
20 Hz
R.F.U.
B
10 Hz
20 Hz
0.1 ΔF/F0
1 s
0.5 s
WT
Doc2α^KO
syt7^KO
C
Asynchronous fraction
Stimulation number
WT
Doc2α^KO
syt7^KO
10 Hz
20 Hz
D
Normalized ΔF/F0 amplitude
Stimulation number
WT
Doc2α^KO
syt7^KO
10 Hz
20 Hz

Figure 4

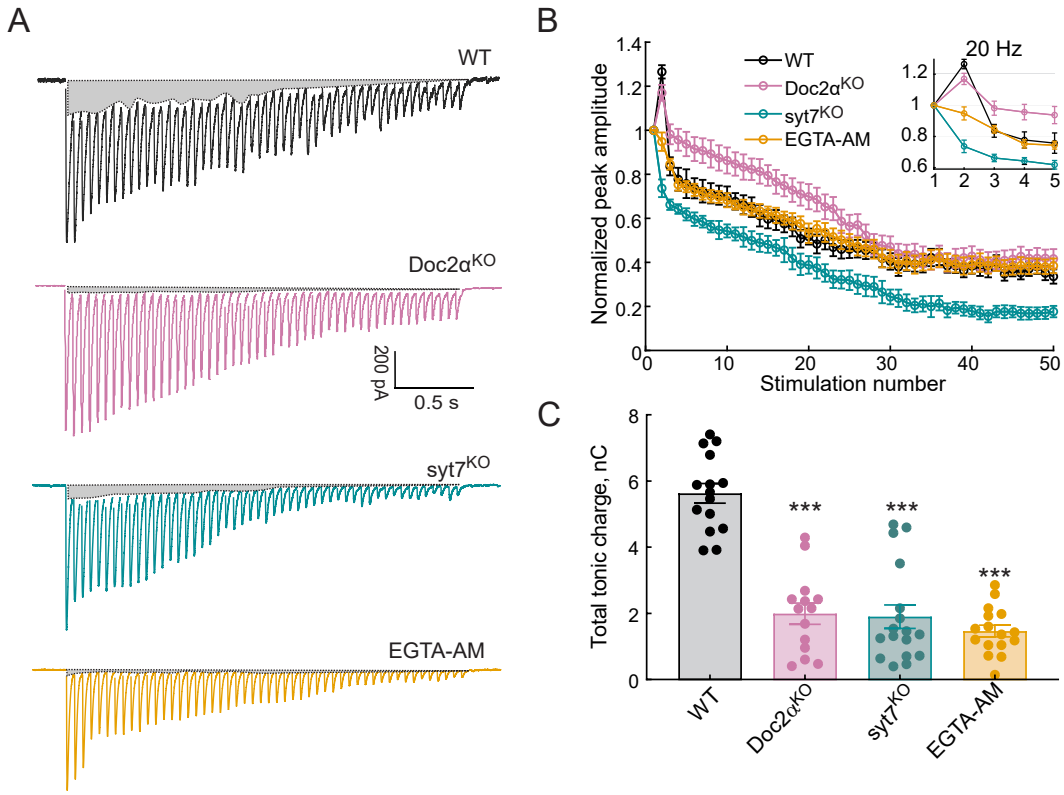
A
WT
Doc2α^KO
200 pA
0.5 s
syt7^KO
EGTA-AM
B
Normalized peak amplitude
Stimulation number
WT
Doc2α^KO
syt7^KO
EGTA-AM
20 Hz
C
Total tonic charge, nC
***
***
***
WT
Doc2αKO
syt7KO
EGTA-AM

Figure 5

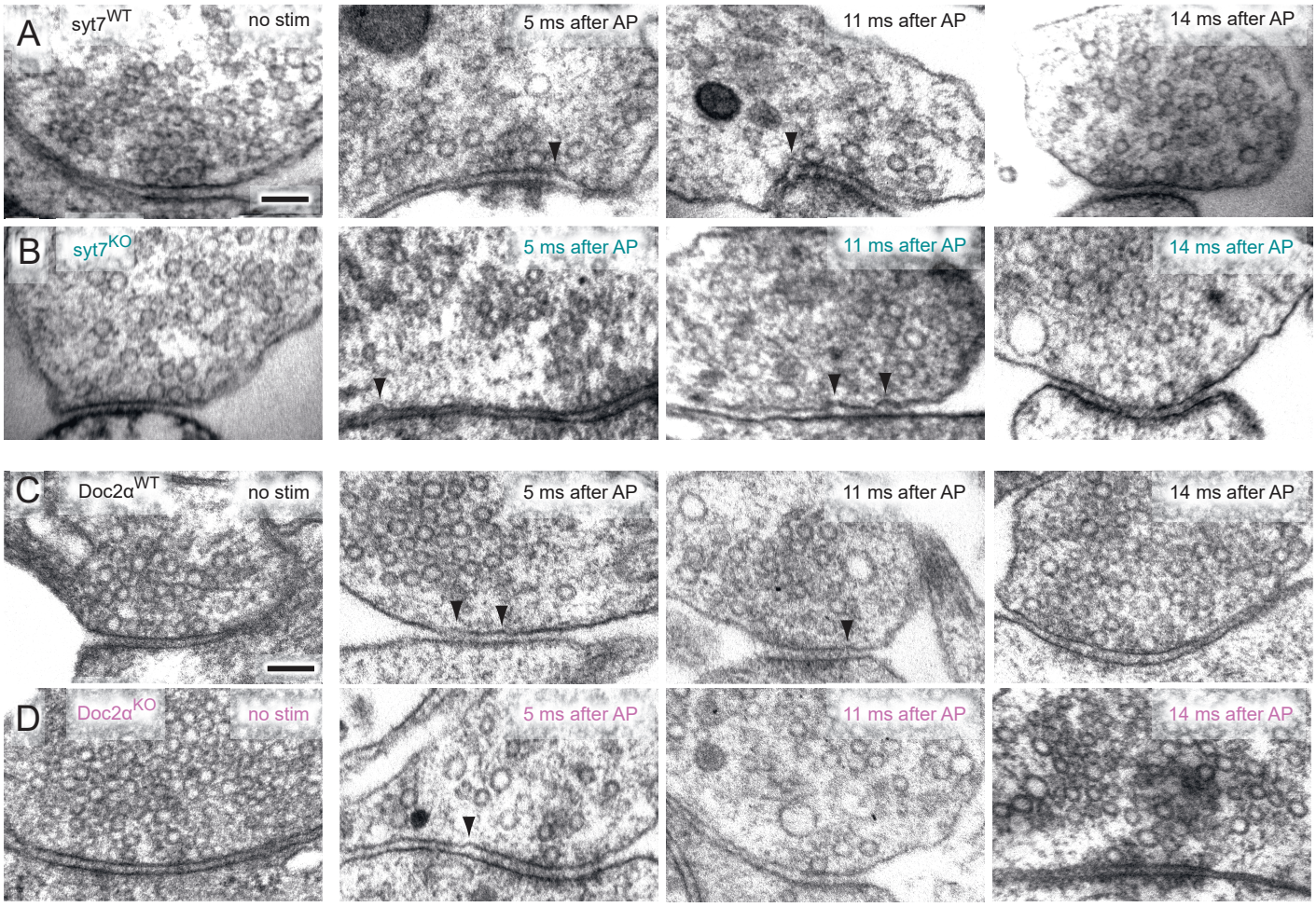

exocytic pits

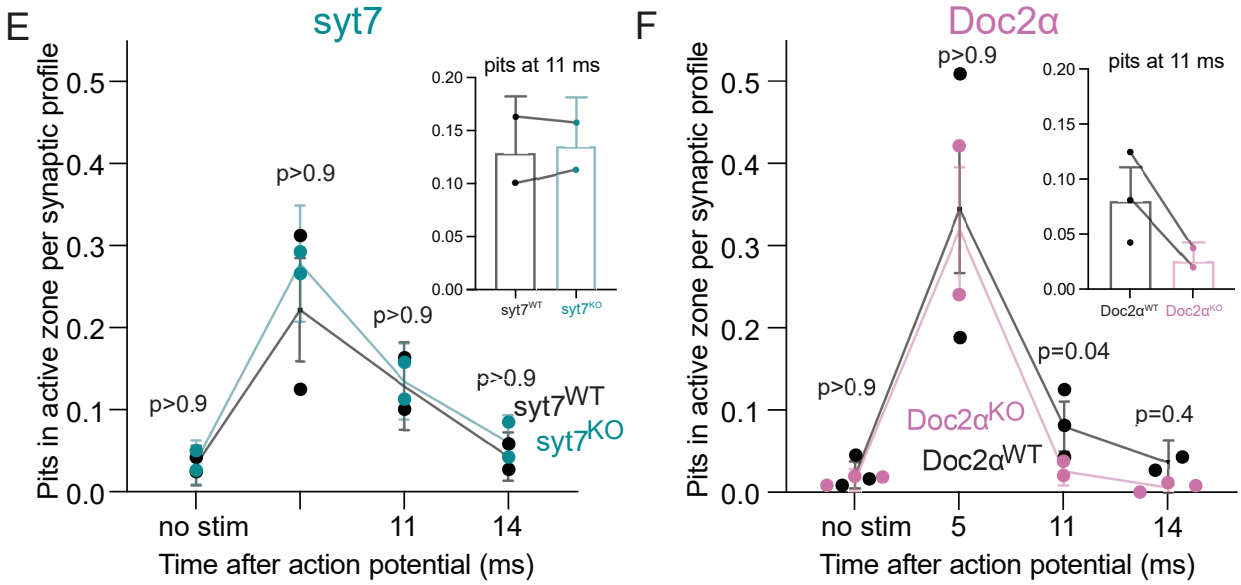

Figure 6

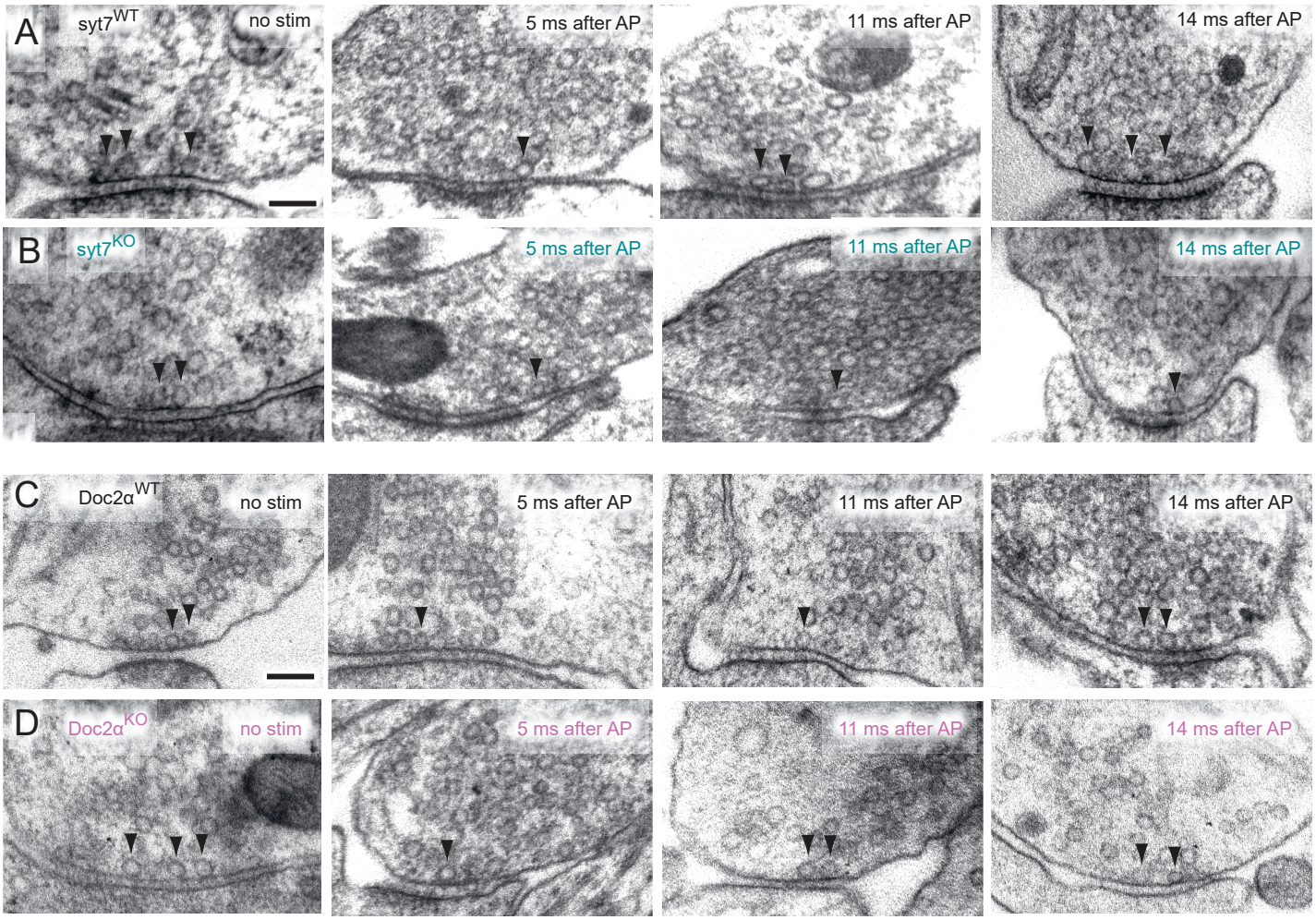
A
syt7WT
no stim
5 ms after AP
11 ms after AP
14 ms after AP
B
syt7KO
5 ms after AP
11 ms after AP
14 ms after AP
C
Doc2αWT
no stim
5 ms after AP
11 ms after AP
14 ms after AP
D
Doc2αKO
no stim
5 ms after AP
11 ms after AP
14 ms after AP

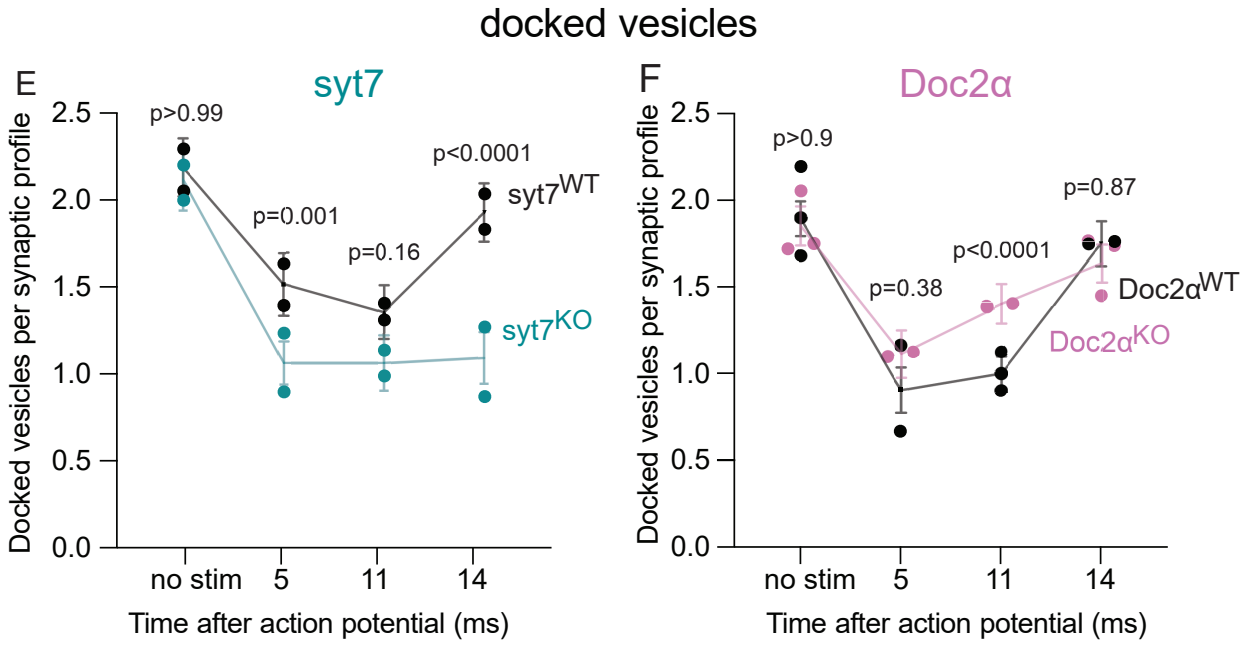
docked vesicles
E
syt7
Docked vesicles per synaptic profile
2.5
2.0
1.5
1.0
0.5
0.0
p>0.99
p=0.001
p=0.16
p<0.0001
syt7WT
syt7KO
no stim
5
11
14
Time after action potential (ms)
F
Doc2α
Docked vesicles per synaptic profile
2.5
2.0
1.5
1.0
0.5
0.0
p>0.9
p=0.38
p<0.0001
p=0.87
Doc2αWT
Doc2αKO
no stim
5
11
14
Time after action potential (ms)

Figure 7

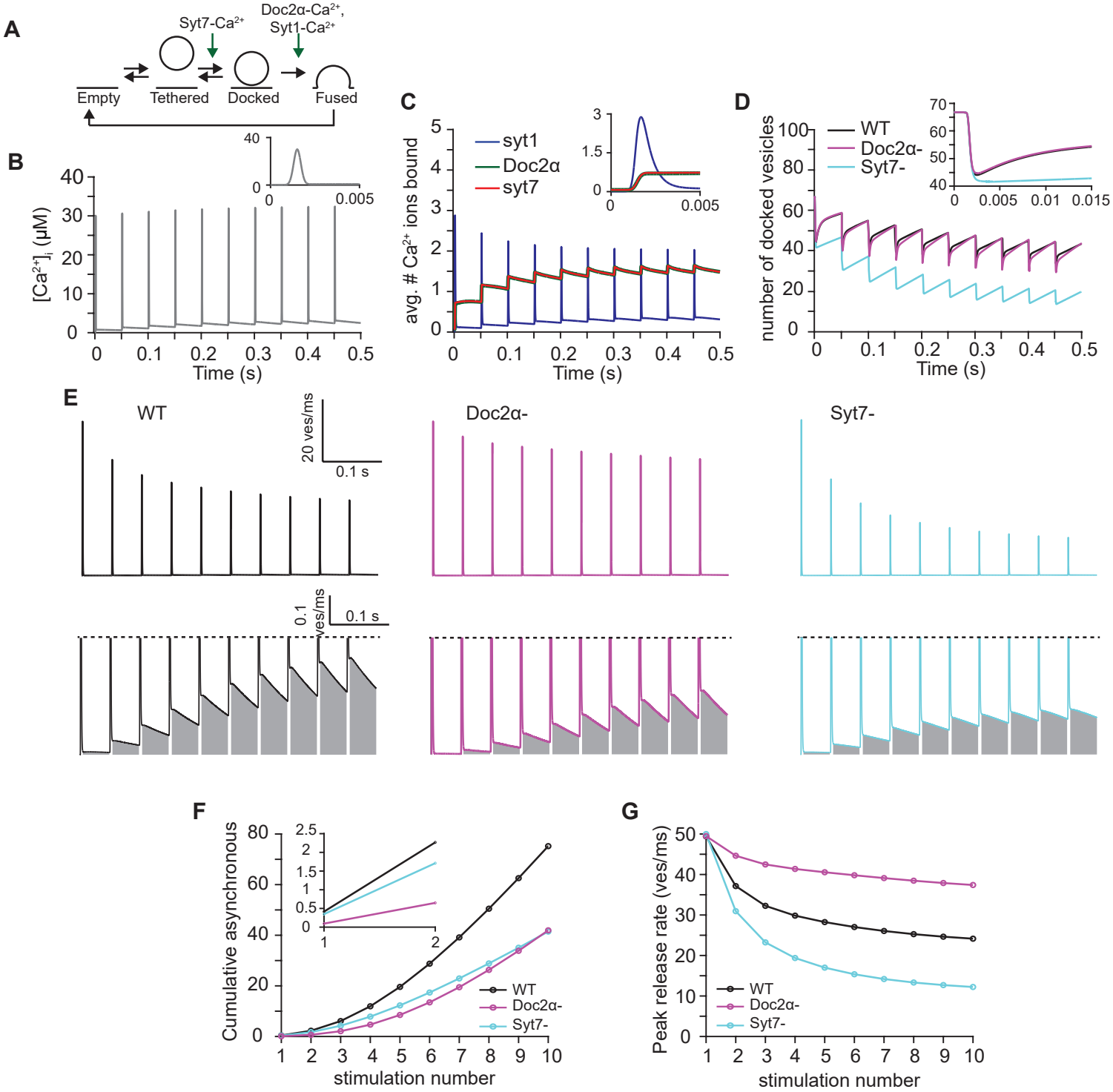
A
Syt7-Ca2+
Doc2α-Ca2+,
Syt1-Ca2+
Empty
Tethered
Docked
Fused
B
[Ca2+]i (μM)
Time (s)
C
avg. # Ca2+ ions bound
syt1
Doc2α
syt7
Time (s)
D
number of docked vesicles
WT
Doc2α-
Syt7-
Time (s)
E
WT
Doc2α-
Syt7-
20 ves/ms
0.1 s
0.1 ves/ms
0.1 s
F
Cumulative asynchronous
stimulation number
WT
Doc2α-
Syt7-
G
Peak release rate (ves/ms)
stimulation number
WT
Doc2α-
Syt7-

Figure 8

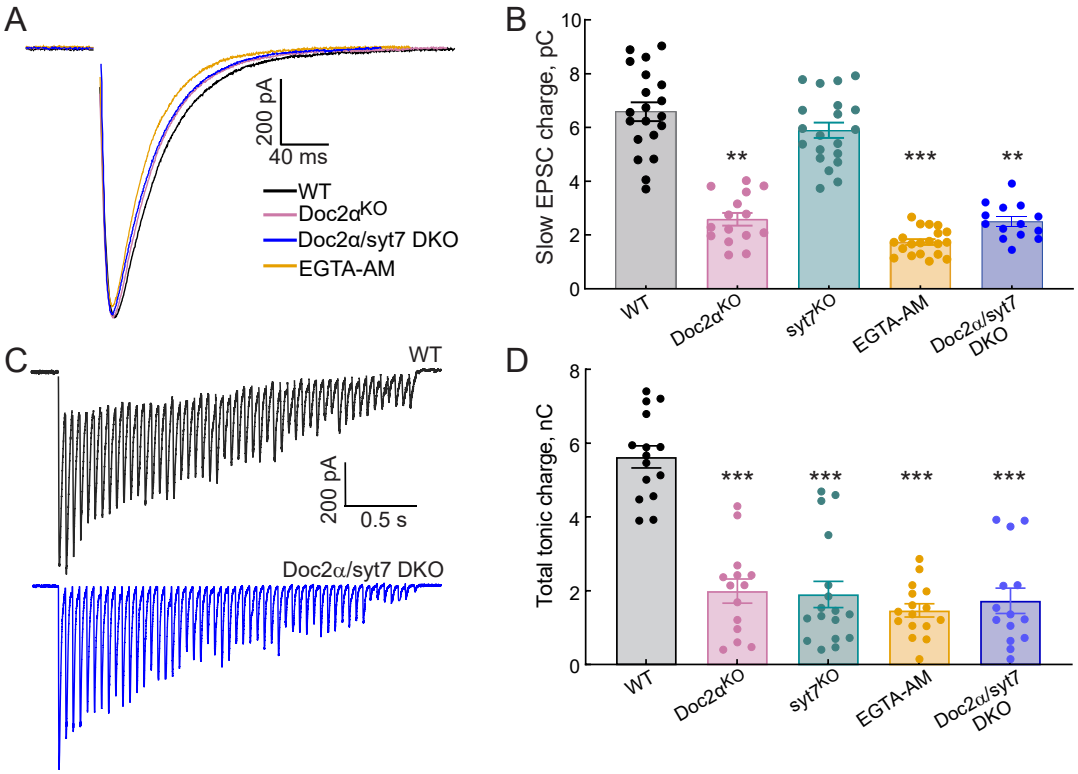
A
200 pA
40 ms
WT
Doc2α^KO
Doc2α/syt7 DKO
EGTA-AM
B
Slow EPSC charge, pC
10
8
6
4
2
0
**
***
**
WT
Doc2α^KO
syt7^KO
EGTA-AM
Doc2α/syt7 DKO
C
WT
200 pA
0.5 s
Doc2α/syt7 DKO
D
Total tonic charge, nC
8
6
4
2
0
***
***
***
***
WT
Doc2α^KO
syt7^KO
EGTA-AM
Doc2α/syt7 DKO